Dynamical inelastic scattering in high-energy electron diffraction and imaging: A new theoretical approach

Z. L. Wang*
Cavendish Laboratory, University of Cambridge, Madingley Road, Cambridge, CB3 0HE, United Kingdom and Department of Physics, Arizona State University, Tempe, Arizona 85287-1504
(Received 13 November 1989)

A generalized multislice theory is proposed from quantum mechanics to approach the multiple elastic and multiple inelastic scattering of high-energy electrons in a solid. The nonperiodic structure of crystals can be introduced in the calculations for the scattering geometries of transmission electron microscopy and reflection electron microscopy. Detailed applications of this generalized theory will be given for calculating (a) the energy-filtered-plasmon energy-loss diffraction patterns and images, (b) the energy-filtered diffraction patterns from atomic inner-shell losses, and (c) the contribution of thermal diffuse scattering to the high-angle annular-dark-field (ADF) scanning-transmission-electron-microscopy (STEM) lattice images. An "incoherent" imaging theory is presented for simulating the ADF STEM images and the detailed calculations are addressed for Ge/Si interfaces.

I. INTRODUCTION

Electron inelastic scattering, as a general phenomenon in high-energy electron diffraction, has been widely used in investigating the structures of materials. The early theory of describing the creation and scattering of high-energy inelastic waves in a crystal was due to Yoshioka.[1] Based on quantum-mechanical theory, he derived a set of coupled Schrödinger equations by considering all the transitions among the ground state and the excited states of the crystal. Due to the complicated coupling between those equations, a proper method has not been established to solve all the inelastic components for a general crystal structure with defects. Some work has been done to consider the effect on the elastic wave of inelastic scattering under the first-order approximation. Besides the crystal potential of atomic arrangement, Yoshioka[1] predicted that there is a real addition to the crystal potential from virtual inelastic scattering as well as an imaginary absorption correction. The corrections due to single-electron excitation were calculated using the Thomas-Fermi atomic model[1] and atomic wave functions.[2] This correction has also been calculated by Humphreys and Hirsch[3] for different inelastic excitation processes. The contribution due to plasmon scattering was studied by Radi[4] and Yoshioka and Kainuma.[5] It is shown by Wang[6] that all the effects to elastic scattering of all the inelastic processes (single-electron excitation, plasmon excitation, and phonon excitation) can be characterized by a complex potential in the multislice approach, which is related to the generalized dielectric response function of the solid.

The first attempt of solving the inelastic waves from Yoshioka's coupling equations was initiated by Howie.[7] Based on the Bloch-wave approach with use of the small-angle approximation, he gave an analytical solution for phonon excitations under some simplified conditions. He also showed that the plasmon scattering preserves the imaging contrast of the elastic scattering. By neglecting the transitions among the excited states, this Bloch-wave approach has been extensively applied to phonon excitations.[8,9] Serneels *et al.*[10] have proposed an iteration method for solving Yoshioka's coupling equations based on the Bloch-wave approach, which assumes the periodic structures of the crystal. So far, there is not a method available which can solve the Yoshioka's coupling equations for a general solid structure considering all the possible transitions.

In this paper we present a new theoretical approach which can solve the coupling Schrödinger equations for a non-periodic crystal by considering all the possible transitions. The detailed theories will be developed for calculating (a) the energy-filtered-plasmon energy-loss diffraction patterns and images in the geometry of reflection electron microscopy (REM), (b) the energy-filtered diffraction patterns from atomic core shell losses, and (c) the contribution of thermal diffuse scattering (TDS) to the high-angle annular-dark-field (ADF) scanning-transmission-electron-microscopy (STEM) lattice images. An "incoherent" imaging theory will be derived for simulating ADF STEM images and some calculated results will be presented for Ge/Si(100) interfaces.

II. MULTISLICE APPROACH TO ELASTIC SCATTERING: AN INTRODUCTION

The multislice method, as a dynamical theory for calculating high-energy electron scattering in a crystal, has been very successfully applied in imaging simulations of high-resolution transmission electron microscopy (HRTEM). This theory was initiated by Cowley and Moodie[11] based on the physical-optics approach. This theory was shown to be equivalent to quantum mechanics.[12,13] For the convenience of our discussion, it is

necessary to review this theory.

Assuming a crystal is cut into slices in the direction perpendicular or almost perpendicular to the incident-beam azimuth, for a high-energy electron beam of about 100 keV, by neglecting the backscattering of the electrons from each slice with use of the small-angle approximation, the elastic wave going into the mth crystal slice and coming out of the slice (see Fig. 1) is related by Eq. (1),[11]

$$\psi_{m+1}(\mathbf{b})=[\psi_m(\mathbf{b})q_0(\mathbf{b})]*P_0(\mathbf{b}) , \tag{1a}$$

where $\mathbf{b}=(x,y)$ in the slice plane, q_0 is the so-called phase-grating function of the slice, $*$ indicates a convolution operation, and P is the propagation function of the wave in the vacuum for a distance $\Delta z=z_{m+1}-z_m$,

$$q_0(\mathbf{b})=\exp\left[i\sigma_0\int_{z=z_m}^{z=z_{m+1}}dz\ U(\mathbf{b},z)\right] , \tag{1b}$$

where U is the atomic potential distribution in the space, which can be different for different atomic layers,

$$P_0(\mathbf{b})=\frac{1}{i\Delta z\lambda_0}\exp(i\pi b^2/\lambda_0\Delta z) , \tag{1c}$$

and

$$\sigma_0=\frac{\pi}{\lambda_0 V_0} . \tag{1d}$$

λ_0 is the wavelength of the electrons with energy E_0 and V_0 is the accelerating voltage of the microscope. Equation (1) is the exact solution of the Schrödinger equation after neglecting the back scattering when Δz approaches zero.[12,13]

The multislice theory described by Eq. (1) has one of the greatest advantages, that is, the atomic arrangement within a slice or in different slices can be in arbitrary arrangement, so that the theory can be easily applied to approach any crystal defects and imperfections in the different scattering geometries. This theory has been applied currently to simulate the high-resolution transmission-electron-microscopy images, convergent-beam electron diffraction (CBED) patterns [Fig. 2(a)],[14] surface profile images in HRTEM [Fig. 2(b)],[15] reflection-electron-microscopy (REM) images, and reflection high-energy electron diffraction (RHEED) patterns at glancing-angle incidence [Fig. 2(c)].[16,17]

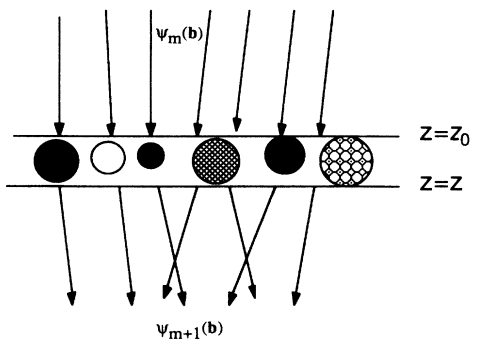

FIG. 1. A schematic diagram illustrating the elastic wave before and after transmission through a crystal slice.

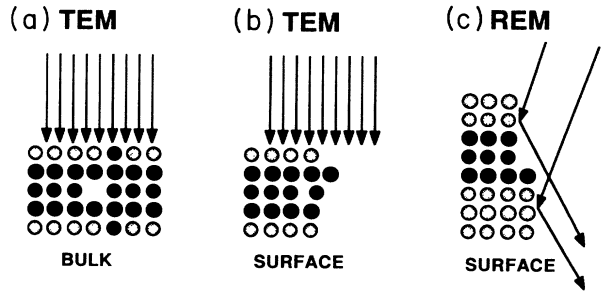

FIG. 2. Application of the multislice theory for simulating (a) the atomic high-resolution transmission electron microscopy (HRTEM) images and convergent beam electron diffraction (CBED) patterns, (b) profile images of surface atomic reconstructions in HRTEM, and (c) reflection electron microscopy (REM) images and reflection high-energy electron diffraction (RHEED) patterns.

To demonstrate the beauty of this theory, Fig. 3 shows a simulated large-angle convergent-beam electron diffraction pattern (LA CBED) pattern of Si(100). The incident-beam disk is chosen so large (with half conical angle 3°) that the interference of the electrons gives the nice Kossel pattern of the crystal, which is obviously related to the crystal structures. This theory gives the convenience of tracing electron scattering depth by depth, then its scattering process can be captured.

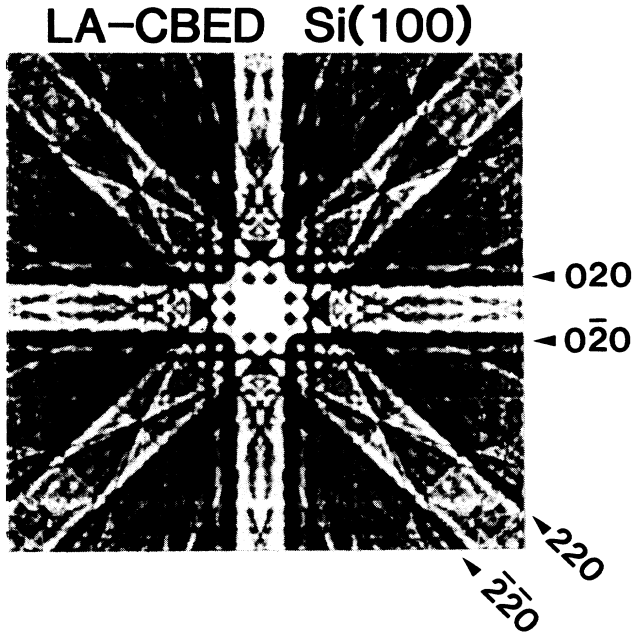

FIG. 3. Simulated large-angle convergent beam electron diffraction LA CBED Kossel pattern of Si(100) for 100-kV electrons, with half-conical angle 6° and specimen thickness 271.5 Å.

As limited by the basis of Eq. (1), however, it is only an elastic scattering theory, no inelastic effect is included in the calculation. Then it cannot be applied to simulate the diffractions of electrons in thicker specimens, which usually involve a large amount of inelastic scattering. Electron inelastic scattering is usually classified as three different processes. Plasmon (or valence) excitation, which characterizes the transitions of electrons from the valence band to the conduction band, involves an energy loss in the range of 5–30 eV and an angular spreading of less than 0.1 mrad for high-energy electrons. More than half of the electrons will loss the energy of a plasmon if the specimen thickness is larger than about 500–1000 Å. This inelastic process is considered as a nonlocalized collective excitation of the electrons in the solid. Atomic core-shell excitations is the second process, which introduces an energy loss in the range of a few hundred to thousands of eV with an angular spreading of an order $\theta_E=\Delta E/2E_0$, where ΔE is the electron energy loss and E_0 is the incident electron energy. This process is considered as the localized excitation and happens only when the impact parameters of the electron are in the size of a subatom. Thermal diffuse scattering (TDS), as the other inelastic process, does not introduce any significant energy loss (less than 0.2 eV) but produces large momentum transfers, which scatters the electrons to higher angles and form Kikuchi lines after further elastic scattering. This process is associated with the vibration of crystal lattices.

It seems that these different inelastic processes have different characteristics, each of them arises from the different interaction of the electrons with the solid. To contain all these effects in the calculations, we need to consider a generalized interaction of an electron with the crystal and the associated scattering. It is necessary to derive a generalized multislice approach for electron diffraction and imaging. This is the purpose of Sec. III.

III. GENERAL SOLUTION OF THE YOSHIOKA'S COUPLING EQUATIONS IN THE MULTISLICE SCHEME

To approach the inelastic scattering properly, one follows Yoshioka's method for deriving the coupling equations, which describe the transitions of the electrons among different states of the crystal. When one considers the interaction of an incident electron with a solid, the Schrödinger equation of the system is

$$\left[-\frac{\hbar^2}{2m_0}\nabla^2+H_c+H'\right]\Phi=E\Phi\ , \tag{2}$$

where $-(\hbar^2/2m_0)\nabla^2$ is the kinetic energy of the electron, H_c is the crystal Hamiltonian, and H' describes the interaction between the electron and the solid, $\Phi(\mathbf{r},\mathbf{r}_1,\ldots,\mathbf{r}_M)$ is the wave function of the system, which depends on $\mathbf{r}$, the coordinates of the incident electron, and on $\mathbf{r}_1,\ldots,\mathbf{r}_M$, the coordinates of the electrons and ions of the crystal. Neglecting exchange effects one can write

$$\Phi(\mathbf{r},\mathbf{r}_1,\ldots,\mathbf{r}_M)=\sum_n a_n(\mathbf{r}_1,\ldots,\mathbf{r}_M)\Psi_n(\mathbf{r})\ , \tag{3}$$

where a_n is the wave function of the crystal in its nth excited state of energy ε_n so that

$$H_c a_n=\varepsilon_n a_n\ . \tag{4}$$

Ψ_0 in Eq. (3) describes the elastic scattered wave of energy $E_0=E$ and Ψ_n describes the inelastically scattered wave of energy $E_n=E-\varepsilon_n$, with $n=1,2,\ldots,m$. Substituting Eqs. (3) and (4) into Eq. (2), multiplying by a_n^*, and integrating over the coordinates $\mathbf{r}_1,\ldots,\mathbf{r}_M$, one obtains,

$$(\nabla^2+k_0^2)\Psi_0=\sum_m\frac{2m_0}{\hbar^2}H'_{0m}(\mathbf{r})\Psi_m\ , \tag{5a}$$

$$(\nabla^2+k_n^2)\Psi_n=\sum_m\frac{2m_0}{\hbar^2}H'_{nm}(\mathbf{r})\Psi_m\ , \tag{5b}$$

where

$$k_n^2=\frac{2m_0}{\hbar^2}E_n\ , \tag{5c}$$

and

$$H'_{nm}=\int a_n^* H' a_m\, d\mathbf{r}_1,\ldots,d\mathbf{r}_M\ . \tag{5d}$$

These are the Yoshioka's coupling equations for inelastic scattering. The summation of m is for all the excited states and the ground state. Our goal is to find the multislice solution of these equations. For convenience of the analysis, we write (5a) and (5b) in the matrix form

$$\nabla^2\begin{bmatrix}\Psi_0\\ \Psi_1\\ \vdots\\ \Psi_m\end{bmatrix}+\begin{bmatrix}k_0^2\Psi_0\\ k_1^2\Psi_1\\ \vdots\\ k_m^2\Psi_m\end{bmatrix}=\frac{2m_0}{\hbar^2}\begin{bmatrix}H'_{00} & H'_{01} & \cdots & H'_{0m}\\ H'_{10} & H'_{11} & \cdots & H'_{1m}\\ \vdots & \vdots & \vdots & \vdots\\ H'_{m0} & H'_{m1} & \cdots & H'_{mm}\end{bmatrix}\times\begin{bmatrix}\Psi_0\\ \Psi_1\\ \vdots\\ \Psi_m\end{bmatrix}\ . \tag{6}$$

Equation (6) is an inhomogeneous equation. The H' matrix is a $m\times m$ transition matrix. By defining $\Psi_n=\exp(i\mathbf{k}_n\cdot\mathbf{r})\phi_n$, using the Green-function method, and assuming $\varepsilon_n\ll E_0$, (6) can be written in the form of (7) (see Appendix A),

$$\begin{bmatrix}\phi_0(\mathbf{r})\\ \phi_1(\mathbf{r})\\ \vdots\\ \phi_m(\mathbf{r})\end{bmatrix}=I-\int\frac{2m_0}{4\pi\hbar^2}d\mathbf{r}'\begin{bmatrix}F(\mathbf{r}-\mathbf{r}',\mathbf{k}_0) & 0 & \cdots & 0\\ 0 & F(\mathbf{r}-\mathbf{r}',\mathbf{k}_1) & \cdots & 0\\ \vdots & \vdots & \vdots & \vdots\\ 0 & 0 & \cdots & F(\mathbf{r}-\mathbf{r}',\mathbf{k}_m)\end{bmatrix}$$
$$\times\begin{bmatrix}H'_{00}(\mathbf{r}') & H'_{01}(\mathbf{r}') & \cdots & H'_{0m}(\mathbf{r}')\\ H'_{10}(\mathbf{r}') & H'_{11}(\mathbf{r}') & \cdots & H'_{1m}(\mathbf{r}')\\ \vdots & \vdots & \vdots & \vdots\\ H'_{m0}(\mathbf{r}') & H'_{m1}(\mathbf{r}') & \cdots & H'_{mm}(\mathbf{r}')\end{bmatrix}\begin{bmatrix}\phi_0(\mathbf{r}')\\ \phi_1(\mathbf{r}')\\ \vdots\\ \phi_m(\mathbf{r}')\end{bmatrix}, \tag{7a}$$

where I is an "unit" matrix defined as

$$I=\begin{bmatrix}1\\ 1\\ \vdots\\ 1\end{bmatrix}. \tag{7b}$$

F is defined as

$$F(\mathbf{r}-\mathbf{r}',\mathbf{k}_n)=\frac{\exp[i(k_n|\mathbf{r}-\mathbf{r}'|-\mathbf{k}_n\cdot(\mathbf{r}-\mathbf{r}'))]}{|\mathbf{r}-\mathbf{r}'|}. \tag{7c}$$

When the high-energy electron scattering satisfies the conditions (i) $\alpha^2\ll 1$, where α is the scattering angle, this is called the small-angle approximation; and when it satisfies (ii) $|\mathbf{r}-\mathbf{r}'|\approx z-z'$, this is called the nondeflection approximation. Neglecting the back scattering, condition (ii) is equivalent to

$$k_n|\mathbf{r}-\mathbf{r}'|-\mathbf{k}_n\cdot(\mathbf{r}-\mathbf{r}')\approx k_n\frac{|\mathbf{b}-\mathbf{b}'|^2}{2(z-z')}.$$

Here $\mathbf{b}=(x,y)$ and $\mathbf{b}'=(x',y')$.

By introducing a propagation function as defined in Eq. (8b), (7a) becomes

$$\begin{bmatrix}\phi_0(\mathbf{b},z)\\ \phi_1(\mathbf{b},z)\\ \vdots\\ \phi_m(\mathbf{b},z)\end{bmatrix}=I+\left[-\frac{i}{\hbar v}\right]\int\int_{z'=-\infty}^{z'=z}\begin{bmatrix}P_0(\mathbf{b}-\mathbf{b}',z-z') & 0 & \cdots & 0\\ 0 & P_1(\mathbf{b}-\mathbf{b}',z-z') & \cdots & 0\\ \vdots & \vdots & \vdots & \vdots\\ 0 & 0 & \cdots & P_m(\mathbf{b}-\mathbf{b}',z-z')\end{bmatrix}$$
$$\times\begin{bmatrix}H'_{00}(\mathbf{b}',z') & H'_{01}(\mathbf{b}',z') & \cdots & H'_{0m}(\mathbf{b}',z')\\ H'_{10}(\mathbf{b}',z') & H'_{11}(\mathbf{b}',z') & \cdots & H'_{1m}(\mathbf{b}',z')\\ \vdots & \vdots & \vdots & \vdots\\ H'_{m0}(\mathbf{b}',z') & H'_{m1}(\mathbf{b}',z') & \cdots & H'_{mm}(\mathbf{b}',z')\end{bmatrix}\begin{bmatrix}\phi_0(\mathbf{b}',z')\\ \phi_1(\mathbf{b}',z')\\ \vdots\\ \phi_m(\mathbf{b}',z')\end{bmatrix}d\mathbf{b}'dz', \tag{8a}$$

where P_n is defined as a propagation function of the electrons with energy E_n,

$$P_n(\mathbf{b},\Delta z)=\frac{1}{i\lambda_n\Delta z}\exp\left[\frac{i\pi b^2}{\lambda_n\Delta z}\right]. \tag{8b}$$

λ_n is the wavelength of the electron with energy E_n and v is the velocity of the electron with energy E.

Equation (8a) is an integration equation. In order to find out the multislice solution of this equation, one needs to derive the relationship between the waves $\phi_n(\mathbf{b},z_0)$ going into a crystal slice at $z=z_0$ and those $\phi_n(\mathbf{b},z)$ after penetrating through the slice at $z=z$ if $\Delta z=z-z_0$ is very small. Now one considers the nth row of the Eq. (8a),

$$\begin{aligned}\phi_n(\mathbf{b},z)&=1+\left[-\frac{i}{\hbar v}\right]\int\int_{z'=-\infty}^{z'=z}P_n(\mathbf{b}-\mathbf{b}',z-z')\sum_m H'_{nm}(\mathbf{b}',z')\phi_m(\mathbf{b}',z')d\mathbf{b}'dz'\\ &=1+\left[-\frac{i}{\hbar v}\right]\int\int_{z''=-\infty}^{z''=z_0}P_n(\mathbf{b}-\mathbf{b}'',z-z'')\sum_m H'_{nm}(\mathbf{b}'',z'')\phi_m(\mathbf{b}'',z'')d\mathbf{b}''dz''\\ &\quad+\left[-\frac{i}{\hbar v}\right]\int\int_{z'=z_0}^{z'=z}P_n(\mathbf{b}-\mathbf{b}',z-z')\sum_m H'_{nm}(\mathbf{b}',z')\phi_m(\mathbf{b}',z')d\mathbf{b}'dz'.\end{aligned} \tag{9}$$

By using the properties[13]

$$\int P_n(\mathbf{b},z)d\mathbf{b}=1 \ , \tag{10a}$$

$$P_n(\mathbf{b}-\mathbf{b}',z-z')=\int_{\Sigma}P_n(\mathbf{b}-\mathbf{b}'',z-z'')P_n(\mathbf{b}''-\mathbf{b},z''-z')d\mathbf{b}'' \ , \tag{10b}$$

where Σ is a plane positioned at z'' between z and z', Eq. (9) can be rewritten as

$$\phi_n(\mathbf{b},z)=\int\left[1+\left[-\frac{i}{\hbar v}\right]\int\int_{z''=-\infty}^{z''=z_0}P_n(\mathbf{b}_0-\mathbf{b}'',z_0-z'')\sum_m H'_{nm}(\mathbf{b}'',z'')\phi_m(\mathbf{b}'',z'')d\mathbf{b}''dz''\right]P_n(\mathbf{b}-\mathbf{b}_0,z-z_0)d\mathbf{b}_0$$
$$+\left[-\frac{i}{\hbar v}\right]\int\int_{z'=z_0}^{z'=z}P_n(\mathbf{b}-\mathbf{b}',z-z')\sum_m H'_{nm}(\mathbf{b}',z')\phi_m(\mathbf{b}',z')d\mathbf{b}'dz' \ . \tag{11}$$

Comparing the first term in (11) with Eq. (9) for $z=z_0$, then (11) can be written as

$$\phi_n(\mathbf{b},z)=\int P_n(\mathbf{b}-\mathbf{b}_0,z-z_0)\phi_n(\mathbf{b}_0,z_0)d\mathbf{b}_0+\left[-\frac{i}{\hbar v}\right]\int\int_{z'=z_0}^{z'=z}P_n(\mathbf{b}-\mathbf{b}',z-z')\sum_m H'_{nm}(\mathbf{b}',z')\phi_m(\mathbf{b}',z')d\mathbf{b}'dz' \ . \tag{12}$$

In order to solve Eq. (11), one expands ϕ_n in the order of $(-i/\hbar v)$,

$$\phi_n(\mathbf{b},z)=\sum_{L=0}^{\infty}\left[-\frac{i}{\hbar v}\right]^L f_L^{(n)}(\mathbf{b},z) \ . \tag{13}$$

By inserting (13) into (12), and by equating the coefficients of $(-i/\hbar v)^L$, one gets

$$f_0^{(n)}(\mathbf{b},z)=\int P_n(\mathbf{b}-\mathbf{b}_0,z-z_0)\phi_n(\mathbf{b}_0,z_0)d\mathbf{b}_0 \ , \tag{14a}$$

$$f_L^{(n)}(\mathbf{b},z)=\int\int_{z'=z_0}^{z'=z}P_n(\mathbf{b}-\mathbf{b}',z-z')\sum_m H'_{nm}(\mathbf{b}',z')f_{L-1}^{(m)}(\mathbf{b}',z')d\mathbf{b}'dz' \ . \tag{14b}$$

If H'_{nm} varies slowly in the region of $\Delta z=(z-z_0)$, and also $k_0\approx k_n$, then the solution of (14) can be proven as (see Appendix B)

$$\begin{bmatrix} f_L^{(0)}(\mathbf{b},z) \\ f_L^{(1)}(\mathbf{b},z) \\ \vdots \\ f_L^{(m)}(\mathbf{b},z) \end{bmatrix}=\frac{1}{L!}\int d\mathbf{b}_0\begin{bmatrix} P_0(\mathbf{b}-\mathbf{b}_0,\Delta z) & 0 & \cdots & 0 \\ 0 & P_1(\mathbf{b}-\mathbf{b}_0,\Delta z) & \cdots & 0 \\ \vdots & \vdots & \vdots & \vdots \\ 0 & 0 & \cdots & P_m(\mathbf{b}-\mathbf{b}_0,\Delta z) \end{bmatrix}$$
$$\times\begin{bmatrix} h'_{00}(\mathbf{b}_0,\Delta z) & h'_{01}(\mathbf{b}_0,\Delta z) & \cdots & h'_{0m}(\mathbf{b}_0,\Delta z) \\ h'_{10}(\mathbf{b}_0,\Delta z) & h'_{11}(\mathbf{b}_0,\Delta z) & \cdots & h'_{1m}(\mathbf{b}_0,\Delta z) \\ \vdots & \vdots & \vdots & \vdots \\ h'_{m0}(\mathbf{b}_0,\Delta z) & h'_{m1}(\mathbf{b}_0,\Delta z) & \cdots & h'_{mm}(\mathbf{b}_0,\Delta z) \end{bmatrix}^L\begin{bmatrix} \phi_0(\mathbf{b}_0,z_0) \\ \phi_1(\mathbf{b}_0,z_0) \\ \vdots \\ \phi_m(\mathbf{b}_0,z_0) \end{bmatrix} , \tag{15}$$

where h'_{nm} is defined as

$$h'_{nm}=\int_{z_0}^{z}H'_{nm}(\mathbf{b},z')dz' \ . \tag{16a}$$

Equation (16a) can be written in a form of (16b) for $(z-z_0)\rightarrow 0$,

$$h'_{nm}\approx H'_{nm}(\mathbf{b},z')\Delta z \ . \tag{16b}$$

Combining (15) and (13), one gets the result shown in (17),

$$\begin{bmatrix}\phi_0(\mathbf{b},z)\\ \phi_1(\mathbf{b},z)\\ \vdots\\ \phi_m(\mathbf{b},z)\end{bmatrix}=\int d\mathbf{b}_0\begin{bmatrix}P_0(\mathbf{b}-\mathbf{b}_0,\Delta z) & 0 & \cdots & 0\\ 0 & P_1(\mathbf{b}-\mathbf{b}_0,\Delta z) & \cdots & 0\\ \vdots & \vdots & \vdots & \vdots\\ 0 & 0 & \cdots & P_m(\mathbf{b}-\mathbf{b}_0,\Delta z)\end{bmatrix}$$
$$\times\exp\left[-\frac{i}{\hbar v}\begin{bmatrix}h'_{00}(\mathbf{b}_0,\Delta z) & h'_{01}(\mathbf{b}_0,\Delta z) & \cdots & h'_{0m}(\mathbf{b}_0,\Delta z)\\ h'_{10}(\mathbf{b}_0,\Delta z) & h'_{11}(\mathbf{b}_0,\Delta z) & \cdots & h'_{1m}(\mathbf{b}_0,\Delta z)\\ \vdots & \vdots & \vdots & \vdots\\ h'_{m0}(\mathbf{b}_0,\Delta z) & h'_{m1}(\mathbf{b}_0,\Delta z) & \cdots & h'_{mm}(\mathbf{b}_0,\Delta z)\end{bmatrix}\right]\begin{bmatrix}\phi_0(\mathbf{b}_0,z_0)\\ \phi_1(\mathbf{b}_0,z_0)\\ \vdots\\ \phi_m(\mathbf{b}_0,z_0)\end{bmatrix}. \tag{17}$$

Equation (17) gives a general relationship between all the elastic and inelastic waves before and after penetrating a crystal slice. The exponential matrix indicates the multiple scattering of the electrons among all these states, the Lth-order expansion term of the exponential matrix described the Lth-order multiple scattering. Equation (17) is actually the multiple elastic and multiple inelastic scattering of the electrons in the crystal, which is essentially a theory of Kikuchi patterns. It can be shown that the total electron intensity before and after penetrating a crystal slice governed by Eq. (17) is conserved (see Appendix C).

In order to get some simplified results, we consider the first-order approximation of (17). Assuming $|H_{nm}|\ll|H_{nn}|$ and $\sigma|H_{nm}|\ll 1$ for $n\neq m$, with $\sigma=1/\hbar v$, then the exponential term of the matrix can be written as a summation of a diagonal matrix and a nondiagonal matrix,

$$\exp(-i\sigma[\cdots])=\exp\left\{i\sigma\left[\begin{bmatrix}h'_{00} & 0 & \cdots & 0\\ 0 & h'_{11} & \cdots & 0\\ \vdots & \vdots & \vdots & \vdots\\ 0 & 0 & \cdots & h'_{mm}\end{bmatrix}+\begin{bmatrix}0 & h'_{01} & \cdots & h'_{0m}\\ h'_{10} & 0 & \cdots & h'_{1m}\\ \vdots & \vdots & \vdots & \vdots\\ h'_{m0} & h'_{m1} & \cdots & 0\end{bmatrix}\right]\right\}. \tag{18}$$

Using the approximation of $h'_{00}\approx h'_{11}\approx\cdots\approx h'_{mm}$, the first matrix is an unit matrix, so that the commutation relationship holds, then

$$\exp(-i\sigma[\cdots])\approx\begin{bmatrix}\exp(-i\sigma h'_{00}) & -i\sigma h'_{01}\exp(-i\sigma h'_{00}) & \cdots & -i\sigma h'_{0m}\exp(-i\sigma h'_{00})\\ \vdots & \vdots & \vdots & \vdots\\ -i\sigma h'_{m0}\exp(-i\sigma h'_{mm}) & -i\sigma h'_{m1}\exp(-i\sigma h'_{mm}) & \cdots & \exp(-i\sigma h'_{mm})\end{bmatrix}. \tag{19}$$

Inserting (19) into (17), one has

$$\begin{bmatrix}\phi_0(\mathbf{b},z)\\ \phi_1(\mathbf{b},z)\\ \vdots\\ \phi_m(\mathbf{b},z)\end{bmatrix}=\begin{bmatrix}\left[\exp(-i\sigma h'_{00})\left[\phi_0(\mathbf{b},z_0)-i\sigma\sum_{n\neq 0}h'_{0n}\phi_n(\mathbf{b},z_0)\right]\right]*P_0\\ \left[\exp(-i\sigma h'_{11})\left[\phi_1(\mathbf{b},z_0)-i\sigma\sum_{n\neq 1}h'_{1n}\phi_n(\mathbf{b},z_0)\right]\right]*P_1\\ \vdots\\ \left[\exp(-i\sigma h'_{mm})\left[\phi_m(\mathbf{b},z_0)-i\sigma\sum_{n\neq m}h'_{mn}\phi_n(\mathbf{b},z_0)\right]\right]*P_m\end{bmatrix}. \tag{20}$$

The physical meaning of Eq. (20) can be described as follows. For the elastic scattered wave ϕ_0, the first term is the phase grating result of the crystal slice, which is the elastic penetration of the incident elastic wave. The terms containing h'_{0n} are the "transitions" of the electrons from the excited states to the ground state. This is effectively the virtual inelastic scattering process in electron diffraction, i.e., the electron loses energy first (inelastic scattering) and then regains the same amount of energy to become "elastic" again. This process can be characterized by a complex correction potential related with the dielectric excitation property of the solid.[6] For the excited states, ϕ_n, the first term is the elastic scattering of the incident inelastic wave in the slice; the h'_{mn} terms are the transitions from the other states, including the ground state, to the nth excited state. This term can be considered as the generation of the inelastic wave when the electron penetrates through the slice. Also it is obvious that Eq. (20) reduces to the multislice formula of elastic scattering, Eq. (1), if all the inelastic transitions vanish, i.e., $h'_{mn}=0$ for $n\neq m$.

If one knows the elastic incident wave before the electron strikes the crystal entrance surface, then all the generated elastic and inelastic waves after the first slice can be calculated through Eq. (20). Then these waves can be taken as the incident waves for the second slice, the

waves after penetrating the second slice can also be calculated through Eq. (20). So all the waves after penetrating through the crystal can be obtained. This is the principle how the multislice theory works.

IV. SPECIAL CASES OF ONLY ONE EXCITED STATE

Let us consider a case of only one excited state. This case happens in most plasmon excitation and single-electron excitations. The crystal can be considered as either in its excited state or in its ground state. By taking $m=1$, through some algebra, Eq. (17) reduces to the following forms:

$$\phi_0(\mathbf{b},z)=\left[\exp(-i\sigma h'_{00})\left[\cos(\sigma|h'_{10}|)\phi_0(\mathbf{b},z_0)-i\sin(\sigma|h'_{10}|)\frac{h'_{01}}{|h'_{01}|}\times\phi_1(\mathbf{b},z_0)\right]\right]*P_0\ ; \quad (21a)$$

$$\phi_1(\mathbf{b},z)=\left[\exp(-i\sigma h'_{11})\left[\cos(\sigma|h'_{10}|)\phi_1(\mathbf{b},z_0)-i\sin(\sigma|h'_{10}|)\frac{h'_{10}}{|h'_{10}|}\times\phi_0(\mathbf{b},z_0)\right]\right]*P_1\ . \quad (21b)$$

Now one can apply Eq. (21) for plasmon losses and single-electron excitations.

A. Case 1: Energy-filtered electron images after exciting a plasmon

In Eq. (21), since

$$\cos(\sigma|h'_{10}|)\approx 1-\frac{(\sigma|h'_{10}|)^2}{2}\approx\exp\left[-\frac{(\sigma|h'_{10}|)^2}{2}\right]$$

for $\sigma|h'_{10}|\ll 1$, then we can define an absorption function μ as given by (22a) and an electron inelastic mean-free path Λ as given by (22b),

$$\mu(\mathbf{b},z_0)=\frac{(\sigma|h'_{10}|)^2}{\Delta z}\ , \quad (22a)$$

$$\Lambda(\mathbf{b},z_0)=\frac{1}{\mu(\mathbf{b},z_0)}\ . \quad (22b)$$

After neglecting the transition of the electron from its excited state to the ground state, then (21b) can be written as

$$\phi_1(\mathbf{b},z)=\left\{\exp(-i\sigma h'_{11})\left[\exp\left[-\frac{\mu\Delta z}{2}\right]\phi_1(\mathbf{b},z_0)-i\sigma h'_{10}\phi_0(\mathbf{b},z_0)\right]\right\}*P_1\ . \quad (23)$$

In (23), the $\exp(-\mu\Delta z/2)$ term describes the absorption effect from the inelastic scattering. For plasmon excitations, h'_{01} may be taken as a product of a complex constant with a real function. In addition using $h'_{00}\approx h'_{11}$, then Eqs. (19a) and (23) can be written in the form of (24) after a proper choice of the constant phase factor of the wave function ϕ_0,

$$\phi_0(\mathbf{b},z)=\left\{q(\mathbf{b})\left[\exp\left[-\frac{\mu\Delta z}{2}\right]\phi_0(\mathbf{b},z_0)\right]\right\}*P_0\ ; \quad (24a)$$

$$\phi_1(\mathbf{b},z)=\left\{q(\mathbf{b})\left[\exp\left[-\frac{\mu\Delta z}{2}\right]\phi_1(\mathbf{b},z_0)+\left[\frac{\Delta z}{\Lambda}\right]^{1/2}\phi_0(\mathbf{b},z_0)\right]\right\}*P_1\ , \quad (24b)$$

where $q(\mathbf{b})$ is defined as the slice transmission function, which is essentially the same as that defined in Eq. (1b),

$$q(\mathbf{b})=\exp(-i\sigma h'_{00})\ . \quad (24c)$$

Equation (24) is the exact form of the theory proposed by Wang,[18,19] based on the physical-optics approach, for calculating the energy-filtered inelastic images. The term $\Delta z/\Lambda$ is the probability of generating the plasmon loss while the electron traveling through the slice. This means that the electron energy loss is a mean process depending on its average traveling distance.

Since plasmon excitation is a process of nonlocalized excitation, the mean-free path of plasmon losses does not depend on the excitation position of the electrons through a thin uniform foil in the TEM geometry. The $\Delta z/\Lambda$ term can then be taken out of the calculation as a constant. The propagation of the electrons after plasmon loss is then almost identical to the elastic scattered electrons. The energy-filtered plasmon-loss images then will preserve the same contrast as that of the elastic scattered electrons in TEM. This agrees with what Howie[7] obtained using the Bloch-wave approach.

In REM geometry [see Fig. 1(c)], however, the situation may be different. Since the excitation probability of a surface plasmon is a function of the distance of the electron beam from the surface, the spatial variation of the $\Delta z/\Lambda$ term becomes important. Λ is derived for a planar interface formed by two semi-infinite media $\underline{a}$ and $\underline{b}$ by use of the relativistic dielectric excitation theory[20] when an electron is traveling parallel to the interface at a distance x from the interface in medium $\underline{b}$. For a narrow energy filter that allows only those electrons which have lost the energy of a *single* plasmon (E_p) in the energy-loss range $E_p-\Delta/2<\Delta E<E_p+\Delta/2$ to pass, then

$$\frac{1}{\Lambda(x,\Delta)}=\int_{E_p-\Delta/2}^{E_p+\Delta/2}d\omega\int_0^{q_c}dq_y\frac{d^2P(\omega,q_y,x)}{d\omega\,dqy}\ , \quad (25a)$$

with

$$\frac{d^2P(\omega,q_y,x)}{d\omega\,dq_y}=\frac{e^2}{2\pi^2\epsilon_0\hbar v^2}\mathrm{Im}\left[F(q_y,x)-\frac{1-\beta^2\epsilon_b}{\epsilon_b\alpha_b}\right]\ , \quad (25b)$$

where $\beta_0=v/c$, $\alpha_{a,b}^2=q_y^2+(\omega/v)^2(1-\beta_0^2\epsilon_{a,b})$, v is the velocity of the electron, ϵ_a and ϵ_b are the dielectric con-

stants of media $\underline{a}$ and $\underline{b}$, respectively, which can be taken as the optical-measurement data for bulk materials. q_c is a scattering-angle cutoff of the plasmon scattering in the reciprocal space. The quantity $F(q_y,x)$ in Eq. (25b) is given as

$$F(q_y,x)=\left[\frac{2\alpha_b^2(\epsilon_a-\epsilon_b)}{\epsilon_a\alpha_b+\epsilon_b\alpha_a}+(\alpha_a-\alpha_b)(1-\epsilon_b\beta_0^2)\right]\times\frac{\exp(-2\alpha_b|x|)}{\epsilon_b\alpha_b(\alpha_b+\alpha_a)} . \quad (25c)$$

The calculations according to Eqs. (24) to Eq. (25) in the REM geometry has been reported before.[18,19] It is shown that the different excitation processes, such as surface plasmon and volume plasmon, are created at different depths from the surface. The energy-filtered image of those losses will give the excitation information of different levels from the surface. Also, the diffraction patterns formed by these plasmon losses show different intensity distributions, which can affect the imaging contrast.

B. Single-electron core-shell excitations

In electron diffraction, another inelastic process is the single-electron excitation, during which an electron is excited from one bound state to another, such as the transition of a 1s electron to an ionization state, which is called the K-edge loss in electron energy-loss spectroscopy (EELS). This single-electron process is closely related to the electronic structures of each individual atoms, the solid-state effect can be taken as a second-order approximation. Equation (21) can be applied to calculate the inelastic wave arising from single-electron core-shell excitations.

The transition matrix of an inelastic transition from the ground state to the nth excited state can be written as Eq. (26),[7]

$$H'_{n0}(\mathbf{r},\mathbf{q})=\exp(-i\mathbf{q}\cdot\mathbf{r})\sum_{\mathbf{g}}H_g^{n0}\exp(i\mathbf{g}\cdot\mathbf{r}) , \quad (26)$$

where $\mathbf{q}$ is the wave vector of the excitation created in the lattice. $\mathbf{g}$ is a vector in the reciprocal lattice. For single-electron excitation, it is possible to use the tight-binding approximation for calculating H_g^{nm}.[2] Following the mathematical procedures given by Landau and Lifshitz,[21] one gets

$$H_g^{nm}=\frac{4\pi e^2}{V}\frac{f_{nm}(\mathbf{g}-\mathbf{q})}{|\mathbf{g}-\mathbf{q}|^2} , \quad (27a)$$

where

$$f_{nm}(\mathbf{K})=\langle n|\exp(-i\mathbf{K}\cdot\mathbf{r})|m\rangle , \quad (27b)$$

and $|n\rangle$ and $|m\rangle$ are the normalized one-electron atomic wave functions. V is the volume of the atom. By considering the contributions of all the atoms in the unit cell locating at $\mathbf{R}_j$ ($j=1,2,\ldots$) to the matrix element at position $\mathbf{r}$, and make use of Eqs. (26) and (27), then

$$H'_{nm}(\mathbf{r},\mathbf{q})=\frac{4\pi e^2}{V_c}\sum_{\mathbf{g}}\sum_j\frac{f_{nm}^j(\mathbf{g}-\mathbf{q})}{|\mathbf{g}-\mathbf{q}|^2}\times\exp[i(\mathbf{g}-\mathbf{q})\cdot(\mathbf{r}-\mathbf{R}_j)] , \quad (28)$$

where V_c is the volume of the unit cell. Equation (28) gives the transition matrix of exciting a single electron from the mth state to the nth state with a momentum transfer $\mathbf{q}$, which is confined in the first Brillouin zone. By expanding the summation of $\mathbf{q}$ into the whole reciprocal space, one gets

$$H_{nm}(\mathbf{r})=4\pi e^2\sum_j\int\frac{f_{nm}^j(\mathbf{q})}{q^2}\exp[i\mathbf{q}\cdot(\mathbf{r}-\mathbf{R}_j)]d\mathbf{q} . \quad (29)$$

Equation (29) gives an expression of the transition matrix elements of a single-electron excitation under the tight-binding approximation. The general calculation of f_{nm}^j involves complicated many-body theory. However, under reasonable approximation, the element f_{nm}^j can be calculated based on hydrogenlike model for some light elements, such as C-K and Si-L ionizations. The f_{nm} can be directly evaluated from the generalized oscillating strength (GOS), i.e.,[22]

$$|f_{nm}|=qa_0\left[\frac{\mathcal{R}}{\Delta E}\int_{E_K}^{E_K+\Delta}d\Delta E\frac{df_k}{d\Delta E}\right]^{1/2} , \quad (30)$$

where $\mathcal{R}=13.6$ eV is the Rydberg energy, a_0 is the Bohr radius, df_k/dE is the GOS per unit energy and E_K is the threshold energy of the ionization edge, Δ is the width of the energy-loss window, and ΔE is the electron energy loss. The analytical expression of the GOS for the K edges of hydrogenlike atoms is given in Eq. (31) for $\Delta E > Z_s^2R$, where Z_se is the effective nuclear charge:[23,24]

$$\frac{df}{d\Delta E}=\frac{256\Delta E(Q'+K_H^2/3+\frac{1}{3})\exp(-2\Theta'/K_H)}{Z_s^4R^2[(Q'-K_H^2+1)^2+4K_H^2]^3[1-\exp(-2\pi/K_H)]} , \quad (31a)$$

where $\Theta'=\arctan^{-1}[2K_H/(Q'-K_H^2+1)]$,

$$Q'=(qa_0/Z_s)^2 \quad (31b)$$

and

$$K_H^2=\Delta E/(Z_s^2R)-1 . \quad (31c)$$

Similarly, the f_{nm} for L-edge ionization can be calculated based on the hydrogen model if one neglects the phase factor.[24] The calculation results for single-electron excitation is given in Sec. VI A.

V. THERMAL DIFFUSE SCATTERING

A. General theory

Thermal diffuse scattering (TDS) involves many excited states of different momentum transfers but the transition probability of each is very small. In this case, one can neglect the inelastic transitions among all these excited states, and also consider the fact that the TDS process does produce large amounts of momentum transfer but almost no energy loss. Then Eq. (20) can be simplified as

$$\phi_0(\mathbf{b},z)=\left[\exp(-i\sigma h'_{00})\times\left[\phi_0(\mathbf{b},z_0)-i\sigma\sum_{n\neq 0}h'_{0n}\phi_n(\mathbf{b},z_0)\right]\right]*P_0\ , \tag{32a}$$

$$\phi_n(\mathbf{b},z)=\{\exp(-i\sigma h'_{00})[\phi_n(\mathbf{b},z_0)-i\sigma h'_{n0}\phi_0(\mathbf{b},z_0)]\}*P_0\ . \tag{32b}$$

Equation (32b) considers only the single phonon process and the multiple inelastic scattering is neglected.

In scanning transmission electron microscopy (STEM), the thermal diffuse scattered electrons of different momentum transfer are added *incoherently* in the diffraction plane (i.e., the detection plane). Since the nth excited state in TDS indicates a process of definite momentum transfer, which is a point in the first Brillouin zone and there is no overlay among these points, the electrons of different momentum transfer in TDS can be added *coherently* in real space, because there is no interference between them after converting back to the reciprocal space. By defining a total TDS wave ϕ^T as a coherent sum of all the TDS waves of different momentum transfers,[25]

$$\phi^T=\sum_n\phi_n\ . \tag{33}$$

From Eq. (6), one has

$$\phi^T(\mathbf{b},z)=\left\{\exp(-i\sigma h'_{00})\times\left[\phi^T(\mathbf{b},z_0)-i\sigma\left[\sum_n h'_{n0}\right]\phi_0(\mathbf{b},z_0)\right]\right\}*P_0\ , \tag{34}$$

where the summation over n means the summation of the TDS waves of different momentum $\mathbf{q}$. Now we determine the transition matrix element h'_{n0} for the case of TDS. Based on quantum-mechanical theory, Takagi[26] gave a perturbation potential of phonon scattering in a monoatomic crystal,

$$U(\mathbf{r})=-i\int\sum_j(\tau\cdot\mathbf{A}_j)f(\tau)\exp[i\tau\cdot(\mathbf{r}-\mathbf{R}_j)]d\tau\ , \tag{35a}$$

where

$$f(\tau)=\frac{\exp[-M(\tau)]}{(2\pi)^3}\int v(\mathbf{r})\exp(-i\tau\cdot\mathbf{r})d\mathbf{r}\ , \tag{35b}$$

$v(\mathbf{r})$ is the atomic potential and M is the Debye-Waller factor,

$$M(\tau)=\tfrac{1}{2}\langle(\tau\cdot\mathbf{A}_j)^2\rangle\ , \tag{35c}$$

where the sum over j is taken over all the atoms in the crystal and τ is a continuous reciprocal lattice vector. The angular brackets denote the time average of the corresponding quantity. Expressing the lattice displacement $\mathbf{A}_j$ in the normal modes with wave vector $\mathbf{q}$ (restricted to the first Brillouin zone), frequencies $\omega(q,t)$, polarization unit vectors $\mathbf{e}_{q,t}$ (where $t=1,2,3$ denotes the three perpendicular polarizations), using the results of Howie[7] and Whelan[27] and assuming the validity of the Einstein model, one has

$$\sum_{n=1}^{\infty}H'_{n0}=-ieA\frac{V_c}{(2\pi)^3}\sum_t\sum_{\mathbf{q}}\sum_{\mathbf{g}}e^{i(\mathbf{g}-\mathbf{q})\cdot\mathbf{r}}(\mathbf{g}-\mathbf{q})_t\times V_{g-q}e^{-M(\mathbf{g}-\mathbf{q})} \tag{36a}$$

and

$$A=\frac{\hbar}{\sqrt{2k_B\theta_E M_a N}}\left[\frac{1}{\exp(\theta_E/T)-1}+1\right]^{1/2}\ , \tag{36b}$$

where V_g is the coefficient of the Fourier expansion of the lattice potential, M_a is the atomic mass, N is the total number of atoms, and V_c is the volume of the crystal. $\theta_E=\hbar\omega/k_B$ is the Einstein temperature and k_B is the Boltzman constant. It is noted that A goes to zero if N is very large. This is the result of conservation of energy, because the energy lost by the incident electron, $\hbar\omega$, equals the total vibration energy of the N atoms. Actually A describes the average vibration amplitude of the atom. The sum over $\mathbf{q}$ in (36a) is on the two-dimensional array of states on the surface σ' for which energy and momentum are conserved (in practice the Ewald sphere). The calculation of (36a) is actually a function of incident beam direction. In the first-order approximation, the radius of the Ewald sphere can be taken as very large, so that the surface of the sphere is approximately a plane in the first Brillouin zone. If the incident beam direction is chosen as z axis, then the double sum of $\sum_{\mathbf{q}}\sum_{g_x}\sum_{g_y}$ is actually an integration in the whole reciprocal space for $\tau=(g_x-q_x,g_y-q_y)$ parallel to the x,y plane. In the multislice approach, atomic vibrations in the z direction (incident beam direction) will not make any contribution to the electron angular spreading in the diffraction plane. Then the polarization direction $\mathbf{e}_{q,t}$ can be related to the x and y directions but with arbitrary *time-dependent* phases of α_x and α_y, because each atom is considered to vibrate independently in the x and the y directions. The time average of α_x (or α_y) is zero. Through the inverse Fourier transform, Eq. (36a) can be changed to (37),

$$\sum_{n=1}^{\infty}h'_{n0}=-eA\left[\exp(i\alpha_x)\frac{\partial}{\partial x}+\exp(i\alpha_y)\frac{\partial}{\partial y}\right]V'(\mathbf{b},\Delta z)\ , \tag{37a}$$

where V' is the integrated crystal potential within the

slice along the beam direction, including the thermal correction,

$$V'(\mathbf{b},\Delta z)=\int_{z_0}^{z} V'(\mathbf{b},z)dz \ . \tag{37b}$$

Finally, inserting (37a) in (34) and considering the perturbation result of the TDS to crystal potential H'_{00}, e.g., adding a Debye-Waller factor in the crystal potential, the relationship between the total TDS wave before and after penetrating a crystal slice is given by Eq. (38), with $\sigma_0=e\sigma$,

$$\phi^T(\mathbf{b},z)=\left\{e^{i\sigma_0 V'(\mathbf{b},\Delta z)}\left\{\phi^T(\mathbf{b},z_0)+i\sigma_0 A\left[\left[\exp(i\alpha_x)\frac{\partial}{\partial x}+\exp(i\alpha_y)\frac{\partial}{\partial y}\right]V'(\mathbf{b},\Delta z)\right]\phi_0(\mathbf{b},z_0)\right\}\right\}*P_0 \ . \tag{38}$$

For the elastic scattered wave, an absorption factor needs to be introduced in order to characterize the absorption effect. One can approximately write Eq. (32a) as (39),

$$\phi_0(\mathbf{b},z)=\left\{e^{i\sigma_0 V'(\mathbf{b},\Delta z)}\exp\left[-\sigma_0^2 A^2\left[\left|\frac{\partial}{\partial x}V'(\mathbf{b},\Delta z)\right|^2+\left|\frac{\partial}{\partial y}V'(\mathbf{b},\Delta z)\right|^2\right]/2\right]\phi_0(\mathbf{b},z_0)\right\}*P_0 \ . \tag{39}$$

Equations (38) and (39) outline the main formula for calculating TDS waves in a monoatomic system, which are the same as the equations derived by Cowley[28] based on the physical-optical approach. For a complicated system consisting of several types of atoms, (38) and (39) may be generalized as

$$\phi^T(\mathbf{b},z)=\{q(\mathbf{b})[\phi^T(\mathbf{b},z_0)+G(\mathbf{b},z_0)\phi_0(\mathbf{b},z_0)]\}*P_0 \ , \tag{40a}$$

$$\phi_0(\mathbf{b},z)=[q(\mathbf{b})\phi_0(\mathbf{b},z_0)]*P_0 \ , \tag{40b}$$

with

$$G(\mathbf{b},z_0)=i\sigma_0\sum_j\left[A_{jx}\exp(i\alpha_x j)\frac{\partial}{\partial x}+A_{jy}\exp(i\alpha_y j)\frac{\partial}{\partial y}\right]\times v'_j(\mathbf{b}-\mathbf{R}_j,\Delta z) \tag{40c}$$

and

$$q(\mathbf{b})=\exp\left[i\sigma_0 V'(\mathbf{b},\Delta z)-\sigma_0^2\left[\left|\sum_j A_{jx}\frac{\partial}{\partial x}v'_j(\mathbf{b}-\mathbf{R}_j,\Delta z)\right|^2+\left|\sum_j A_{jy}\frac{\partial}{\partial y}v'_j(\mathbf{b}-\mathbf{R}_j,\Delta z\right|^2\right]/2\right] . \tag{40d}$$

Here $v'_j(\mathbf{b}-\mathbf{R}_j)$ is the crystal potential of the jth atom located at $\mathbf{R}_j$ in the (x,y) plane; A_{jx} and A_{jy} indicate the mean displacements of the atom in the x and y directions, respectively; $q(\mathbf{b})$ is a defined phase-grating function of the crystal slice including the absorption effect; α_x^j and α_y^j are the time-dependent phases of the x and y vibrations of the jth atom. This assumption of independent x and y components of the vibration should however be adequate for most cases. This random phase treatment may give a better approach to the independent vibrations of each atoms.

It is necessary to point out that the generalized Eq. (40a) has broken one assumption of the Einstein model, which is that each atom may vibrate with different energy determined by the vibration amplitude A_j of the atom. As pointed out by Cowley,[28] however, the phase correlations between the atomic vibrations do not affect their image but their diffraction pattern, because the image of each individual atomic column is not affected by the vibration status of another column of atoms under the first-order approximation. Therefore, the theoretical treatment whether based on the Einstein model or any other models, such as Debye model, will not affect the image simulation.[29]

B. Simplified "incoherent" imaging theory for ADF STEM images

Recent instrumental progress has made it possible to obtain atomic resolution lattice images using the high-angle scattered electrons in a scanning transmission electron microscopy (STEM) if a small probe, less than the size of the unit cell, is used.[30,31] These images are called the annular-dark-field (ADF) STEM images and are sensitive to the atomic numbers of the atoms, because the large-angle scattering can be roughly taken as the scattering from the nuclear. Then it is feasible to make chemical identification of atomic sites using this technique.

The simulation of the ADF images, however, cannot be approached using the elastic scattering theory, because the large-angle scattering comes mainly from thermal diffuse scattering (TDS).[29,30] The random thermal vibrations of the atoms make this process as an incoherent excitation. Equation (40) should be the full dynamic theory for TDS if the elastic waves generated from each slice are added incoherently after penetrating through the crystal. This means that each individual TDS wave created from a different slice has to be considered as a separated streak, which will be elastically scattered through the rest of the crystal individually. In practice, this process takes a huge amount of calculation, which becomes even impossible for a thick specimen. Then it is necessary to seek a simplified theory which can give reasonable accurate results but with much less calculation. This is the goal of Sec. V B 1.

1. Case I: No elastic scattering after the TDS

Equation (40) can be simplified if the elastic scattering of the electrons after being inelastically scattered is neglected. This is a good approximation for thin specimens. In this case, the TDS wave generated from each slice should be added incoherently and the change of the electron angular distribution after TDS, if any, is limited to the ADF detector range. This is a reasonable approximation when the detected signal is given by the integration of the intensities over a wide-angle annular detector. Then the intensity detected by the ADF detector for a probe, centered at $\mathbf{b}_p=(x_p,y_p)$, may be written approximately as Eq. (41) in the single-phonon excitation model:

$$I(\mathbf{b}_p)=\sum_n \int |\Delta\phi_n^T(\mathbf{u},\mathbf{b}_p)|^2 D(\mathbf{u})d\mathbf{u} , \tag{41}$$

where $\Delta\phi_n^T$ is the TDS wave generated from the nth slice (at depth $z_n=n\Delta z$) after converting to the reciprocal space, $\mathbf{u}=(u_x,u_y)$. The summation n means the incoherent adding of intensities of the TDS waves generated from different slices, i.e., the intensity integration over crystal thickness. From Eq. (40a),

$$\Delta\phi_n^T(\mathbf{u},\mathbf{b}_p,z_n)=[G(\mathbf{u},z)*\phi_n^0(\mathbf{u},z_n,\mathbf{b}_p)]P_0(\mathbf{u}) ; \tag{42}$$

here ϕ_n^0 stands for the elastic wave at the nth slice and D is the detection function of the ADF detector,

$$D(\mathbf{u})=\begin{cases}1 & \text{for } u_1<u<u_2\\ 0 & \text{otherwise .}\end{cases} \tag{43}$$

u_1 and u_2 are the inner and outer radii of the ADF detector in the reciprocal space. Inserting Eq. (42) into (41) and use the Fourier transforms of G and ϕ_n, with $|P(\mathbf{u})|=1$, one has

$$I(\mathbf{b}_p)=\sum_n \int d\mathbf{u}\left[\int d\mathbf{q}\, G^*(\mathbf{q},z_n)\int d\mathbf{b}\,\phi_n^{0*}(\mathbf{b}-\mathbf{b}_p,z_n)e^{-i(\mathbf{u}-\mathbf{q})\cdot\mathbf{b}} \times\int d\mathbf{q}' G(\mathbf{q}',z_n)\int d\mathbf{b}'\phi_n^0(\mathbf{b}'-\mathbf{b}_p,z_n)e^{i(\mathbf{u}-\mathbf{q}')\cdot\mathbf{b}'}D(\mathbf{u})\right] , \tag{44}$$

where $\mathbf{q}$ and $\mathbf{q}'$ are the two-dimensional vectors in the reciprocal space. By introducing the inverse Fourier transform of the detector function D and integrating over $\mathbf{u}$, Eq. (44) becomes

$$I(\mathbf{b}_p)=\sum_n \int d\mathbf{b}\, G^*(\mathbf{b},z_n)\phi_n^{0*}(\mathbf{b}-\mathbf{b}_p,z_n) \times\int d\mathbf{b}' G(\mathbf{b}',z_n)\phi_n^0(\mathbf{b}'-\mathbf{b}_p,z_n)D(\mathbf{b}-\mathbf{b}') . \tag{45}$$

This is the detected intensity of the ADF detector for an incident probe centered at $\mathbf{b}_p$. It depends only on the elastic probe function, the localized inelastic generation function, and the detector shape function. In practice, if the ADF detector is large enough so that the scattering of the electrons is still within the detector plane, then (45) is still a good approximation.

Equation (45) can be further simplified if all the TDS electrons are treated *incoherently* and *totally* collected by the detector or if the signal collected by the detector is assumed to be proportional to the total TDS scattering. Under this assumption, the elastic Bragg scattering of the electrons after the inelastic scattering (TDS) will not have any effect on the STEM image simulation. Taking the detection function as a unity, i.e., $D(\mathbf{b}-\mathbf{b}')=\delta(\mathbf{b}-\mathbf{b}')$, then from Eq. (45)

$$I(\mathbf{b}_p)=\sum_n \int d\mathbf{b}|G(\mathbf{b},z_n)|^2|\phi_n^0(\mathbf{b}-\mathbf{b}_p,z_n)|^2 =\sum_n |G(\mathbf{b}_p,z_n)|^2*|\phi_n^0(\mathbf{b}_p,z_n)|^2 . \tag{46}$$

This result is exact if the ADF detector detects all the inelastic scattered electrons even for thick crystals. $|G|^2$ is effectively the scattering cross section of the inelastic process and $|\phi_n^0|^2$ is the distribution of electron current density at depth z, determined by (40b). The summation of n actually is equivalent to the intensity integration over crystal thickness.

For very thin objects, Eq. (46) can be connected with *incoherent imaging theory* in optics. $|\phi_n^0|^2$ can then be equated to the modulus square of the impulse response of the lens (i.e., the intensity distribution of the image of a point object), and G is the transmission function of the object.[4]

2. Modified generation function method

To make a better approximation taking into account the size of the detector in Eq. (46), we try to introduce a modified generation function, which is defined by (47). In the reciprocal space

$$G_{\text{new}}(\mathbf{u},z)=\begin{cases}G(\mathbf{u},z) & \text{for } u_1<u<u_2\\ 0 & \text{otherwise .}\end{cases} \tag{47}$$

This newly defined inelastic generation function drops the Fourier components falling out of the angular range of the ADF detector in the reciprocal space and picks up those remaining. Then the detected intensity can be approximately written as

$$I(\mathbf{b}_p)\approx\sum_n \int d\mathbf{u}|G_{\text{new}}(\mathbf{u},z_n)*\phi_n^0(\mathbf{u},z_n,\mathbf{b}_p)P(\mathbf{u})|^2 . \tag{48}$$

Compared with Eq. (41), we have dropped the detection function D, which is contained in the defined new generation function [Eq. (47)]. Following an analysis similar to that in Sec. V B 1, one has

$$I(\mathbf{b}_p)=\sum_n \int d\mathbf{b}|G_{\text{new}}(\mathbf{b},z_n)|^2|\phi_n^0(\mathbf{b}-\mathbf{b}_p,z_n)|^2$$
$$=\sum_n |G_{\text{new}}(\mathbf{b}_p,z_n)|^2 * |\phi_n^0(\mathbf{b}_p,z_n)|^2 . \quad (49)$$

Compared with Eq. (45), Eq. (49) significantly simplifies the numerical calculation. Equation (49) still holds if the inelastically scattered electrons are elastically scattered to produce Kikuchi patterns within the detector angular range.

It is important to note that the STEM imaging intensity is a convolution of the probe intensity distribution with the square of the inelastic generation function, which is proportional to the scattering cross section of the inelastic process. Then the phase of the generation function drops out. This will provide a great advantage for practical numerical calculations, because the phase of an inelastic transition matrix element is always unknown either theoretically or experimentally. From Eq. (40c),

$$|G_{\text{new}}(\mathbf{b},z)|^2=\sigma_0^2\sum_j \left[|A_{jx}|^2 \left| \frac{\partial}{\partial x} v_j''(\mathbf{b}-\mathbf{R}_j,\Delta z) \right|^2 + |A_{jy}|^2 \left| \frac{\partial}{\partial y} v_j''(\mathbf{b}-\mathbf{R}_j,\Delta z) \right|^2 \right] \times \exp[-\mu(\mathbf{b})\Delta z] . \quad (50)$$

v'' is the atomic potential centered at position $\mathbf{R}_j$ after taking the Fourier components out of the angular range of the detector. It is important to note that the phase coupling of the atomic vibrations drops out in Eq. (50). Then the image simulation will not be affected by assuming the Einstein model, the Debye model, or any other model. This is one of the greatest advantage of the incoherent imaging theory. The accuracy of simulating ADF images using Eqs. (46) and (49) will be examined in Sec. VI B 1.

The contribution from pure elastic scattering to the ADF image, after penetrating through the crystal (the Nth slice), can be expressed as

$$I_{\text{Elas}}(\mathbf{b}_p)=\int d\mathbf{u}|\mathcal{F}(\phi_N^0(\mathbf{b}))|^2 D(\mathbf{u}) , \quad (51)$$

where $\mathcal{F}$ denotes the Fourier transformation of x and y. Then the total detected intensity at position $\mathbf{b}_p$ is a summation of TDS [Eq. (49)] with the elastic scattering [Eq. (51)].

VI. CALCULATION RESULTS

A multislice program for simulating HRTEM images is modified to perform the inelastic calculations. The program flow chart is given elsewhere.[32] In the simulation, a large supercell is chosen in a dimension of 40×40 Å^2, which is separated by 256×256 pixels. The supercell has to be large enough so that the electrons cannot be scattered out of the cell. The slice thickness is chosen as half of the atomic unit cell, i.e., 2.715 Å for Si(100). A coherent incident electron probe is assumed for the following calculations.

A. Simulations of the energy-filtered core-shell loss diffraction patterns

It has been reported by Reimer[33] that the energy-filtered diffraction patterns from core-shell losses can be obtained in a specially designed electron microscopy. This achievement makes it possible to investigate the inelastic scattering processes of different mechanisms. In this section, one uses Eq. (21) and Eqs. (29) to (31) to simulate the energy-filtered L-edge diffraction pattern of Si(100).

In dynamic calculations, the incoherency of the inelastic waves generated from different atomic sites makes the calculation extremely difficult. The incoherency of the waves from different crystal slices can be treated exactly following the method introduced by Doyle.[34] That is, the propagation of the inelastic wave generated from each slice has to be treated as a separated stream, whose scattering through the rest of the crystal has to be calculated individually. The final inelastic intensity is the incoherent *intensity* addition of all these individual waves generated from different slices after elastic penetrating through the crystal. This calculation process is rather lengthy and time consuming. To reduce the computation, Cowley[35] has suggested a method of adding arbitrary phases to the inelastic waves generated from different slices, the continuous buildup of the total inelastic waves are the "coherent" summation of those from different slices with arbitrary phases, the propagation of this total wave can be treated as a single stream. This is a reasonable approximation only if the slice number is large, so that the cross terms of them will cancel one with

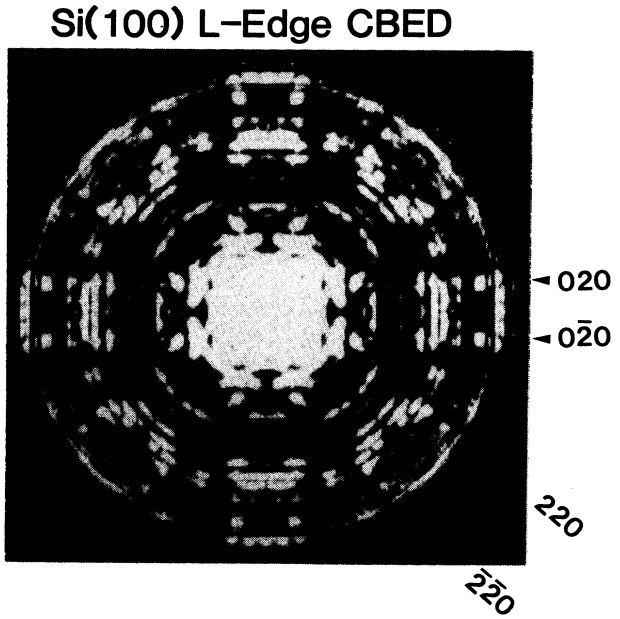

FIG. 4. Simulated energy-filtered Si L-edge core-shell CBED Kikuchi pattern for Si(100), for a specimen thickness 543 Å, beam convergence half-conical angle 12.95 mrad and the energy-loss window $\Delta=5$ eV above the L edge. This calculation was done by adding arbitrary phases to the inelastic waves generated from different slices.

another approximately. Shown in Fig. 4 is a simulated energy-filtered L-edge CBED pattern, with half conical angle 12.95 mrad, of Si(100) according to this treatment. It is important to note that the Kikuchi patterns are formed, which comes from the elastic scattering of the inelastic waves. The interference of the overlap disks gives the nonuniform intensity distribution in the diffraction pattern. The arbitrary phases generated by the computer are not ideally arbitrary, which may give some phase correlation in the diffraction pattern.

The elastic scattering of the inelastic waves produces the Kikuchi patterns. Figure 5 shows a comparison of a simulated CBED of Si(100) for the elastic scattered electrons [Fig. 5(a)] and the electrons after exciting the Si L edge and then being elastically scattered through 543 Å [Fig. 5(b)]. The nice diffraction spot is seen in the elastic CBED pattern. The formation of Kikuchi bands is visible in Fig. 5(b), which comes from the angular spreading of the inelastic scattering.

B. Simulation of high-angle ADF STEM lattice image of Ge/Si interfaces

In STEM image simulation, the incident wave probe, centered at a point $\mathbf{b}_p=(x_p,y_p)$ on the specimen surface, is defined by the objective aperture, i.e.,

$$\phi_0(\mathbf{b},\mathbf{b}_p)=\int A_{\rm ob}(\mathbf{u})\exp[-2\pi\mathbf{u}\cdot(\mathbf{b}-\mathbf{b}_p)-iW(\mathbf{u})]d\mathbf{u}\ ; \tag{52a}$$

where

$$A_{\rm ob}(\mathbf{u})=\frac{1}{1+\exp[(u^2-u_{\rm ap}^2)/\delta_{\rm ap}]} \tag{52b}$$

and

$$W(\mathbf{u})=\pi\lambda_0 u^2(C_s\lambda_0^2u^2/2-\Delta f)\ . \tag{52c}$$

Here C_s is the spherical aberation of the objective lens, and Δf is the defocus value. $\delta_{\rm ap}$ is a small quantity for smoothing the edge of the aperture. In the following calculation, $u_{ap}=0.5$ Å^{-1} (18.5 mrad), $V=100$ kV, $C_s=0.8$ mm, $\delta_{\rm ap}=0.002$ Å^{-1}, and $\Delta f=800$ Å unless it is specified. This gives a probe shape of about 1.2 Å in half-width. To reduce the interacting CPU time, one calculates only a line scan of the electron probe across the Ge/Si boundary through the atomic centers. For simplicity of the calculation, the Ge and Si lattice are assumed to be matched coherently at the boundary and both of the materials have the same lattice constant. The beam incident azimuth was chosen as [100]. The atomic scattering factor is taken in the form of Mott formula,

$$f(s)=0.023\,934\frac{Z-f_x(s)}{s^2}\ , \tag{53}$$

where $s=u/2$, Z is the atomic number, and f_x is the x-ray scattering factor for this atomic number. Also, a proper Debye-Waller factor has been added to the scattering factor of each atom according to the assumed mean vibration amplitude. This can significantly affect the relative contrast of each atom in the ADF images.

1. *Accuracy of using Eqs. (46) and (49) for ADF image simulations*

The quantitative simulation of ADF images involves the treatment of incoherency of the TDS waves generated from different crystal slices if all the atoms are vibrating completely randomly. The vibration correlation of the neighboring atoms will not affect the image simulation according to Wang and Cowley,[29,32] therefore the atoms within the same slice can be assumed to vibrate as a whole in a sheet. To process the incoherent calculation accurately, one has to calculate the TDS wave generated

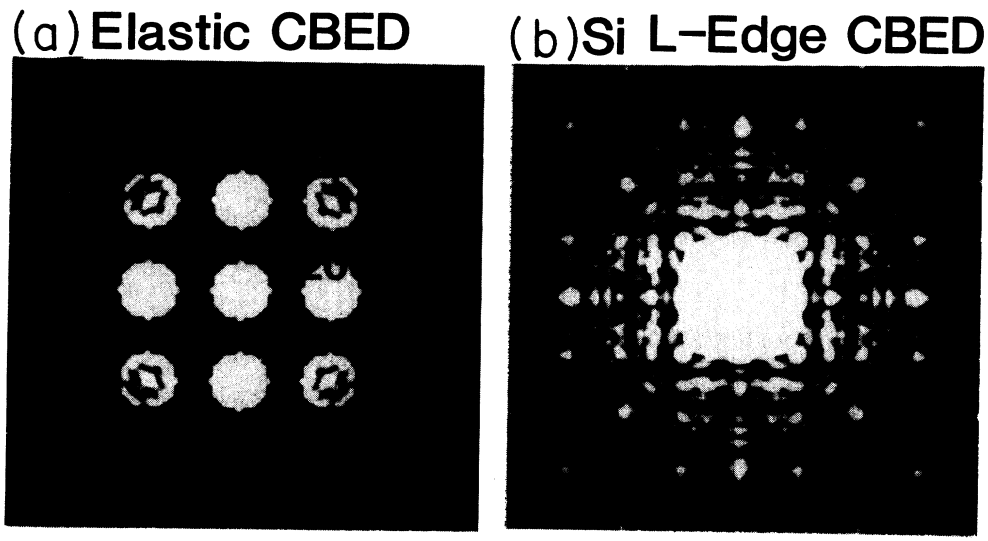

FIG. 5. Simulated Si(100) CBED patterns from (a) elastic scattered electrons and (b) electrons after exciting the Si L edge and then being elastically scattered for 543 Å to form the Kikuchi pattern. The beam convergence half-conical angle is 5.55 mrad and the energy-loss window is $\Delta=5$ eV above the L edge.

from different slices and let them be scattered elastically through the rest of the crystal thickness individually, then add the *intensities* of each individual TDS components generated from different slices after penetrating through the crystal. This calculation process considers the incoherency of the inelastic scattering precisely but involves huge amounts of calculations. This is the exact result of dynamic scattering theory of Eq. (40), which should apply to crystals of any thickness if only a single phonon process is considered.

The simplified methods, described in Eqs. (46) and (49), can greatly reduce the amounts of calculation, but the accuracy of this treatment has to be examined. Shown in Fig. 6(a) is a comparison of the calculated ADF image across the Ge/Si boundary using the theory of full dynamic incoherent scattering (described in the last paragraph) (curve *A*), Eq. (49) (curve *B*), and Eq. (46) (curve *C*). Different intensity levels are obtained for the different equations, but each of the curves shows almost the same variation tendency. To see the relative contrast variation of the Ge and Si atoms, the three curves are normalized at the Ge site and compared in Fig. 6(b). It is surprising to note that the three curves show almost the same contrast variations. The contrast difference between them is less than 5%. This gives the answer that the simulation based on either Eq. (46) or Eq. (49) can give almost the accurate contrast distribution of the ADF image for a thin crystal. This important result shows that the incoherent imaging theory can be used to simulate the ADF imaging contrast quantitatively if the image intensity is dominated by TDS.

It may be noticed that the Si atom closest to the Ge boundary has higher contrast than the next Si atom. This may come from the contribution of the tail of the probe scattering from the Ge or from a spreading of the probe in the crystal due to the discontinuity at the interface. Then it is possible that an error of one monolayer may be made in the chemical identifications.

It is important to emphasize that the incoherent inelastic scattering can give atomic resolution *lattice images*. The mechanism is obviously different from the coherent TEM or STEM imaging theory. The simulations described in Sec. VI B 2 are carried out using Eq. (49) by considering the contribution of the TDS electrons only.

2. *Dependences of ADF imaging contrast on the size of the ADF detector, the focus of the objective lens, and the specimen thickness*

ADF STEM imaging contrast depends on the size of the ADF detector. Shown in Fig. 7 is a comparison of the simulated pure TDS ADF image [according to Eq. (49)] across the Ge/Si(100) interface for different angular collecting ranges of the ADF detector. The TDS electron around the center diffraction disk ($\beta < 37$ mrad) gives almost an uniform intensity at each atomic sites, where β is the collection angle of the detector in the diffraction plane. When the collecting angle goes higher to $37 < \beta < 74$ mrad, a large amount of TDS electrons come into the detector and show atomic resolution. It is obvious that the Ge atoms have stronger contrast compared to the Si atoms. But the contrast does not follow the rule of proportionality to Z^2, as expected from a model of single-atom Rutherford scattering. If the detector angle goes even higher to $74 < \beta < 111$ mrad, the image intensity starts to drop off. It is obvious that most of the TDS

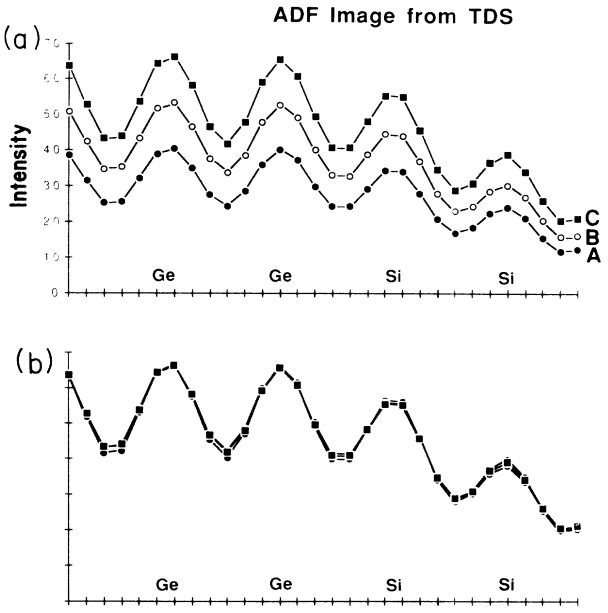

FIG. 6. (a) A comparison of the simulated ADF image intensity across the Ge/Si interface using the full dynamical incoherent scattering theory (i.e., consider the elastic scattering of the electrons after being inelastic scattered) (curve *A*), simplified incoherent imaging theory Eq. (49) (curve *B*), and Eq. (46) (curve *C*). (b) is a comparison of the three curves shown in (a) after being normalized at the Ge sites. This is to test the accuracy of simulated imaging contrast by use of the simplified theory. The specimen thickness is 108.3 Å. The mean displacements of the Ge and Si atoms are taken as 0.1 Å.

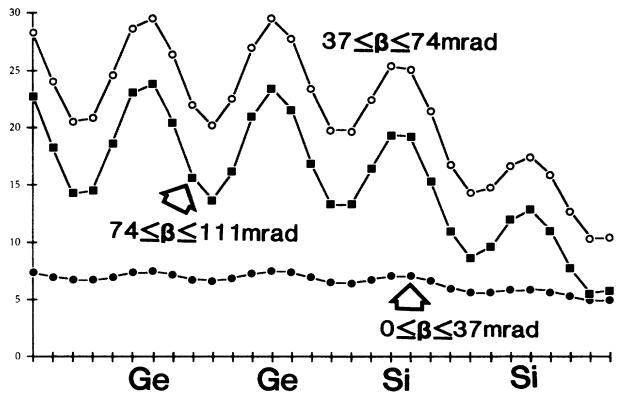

FIG. 7. Dependence of the high-angle ADF STEM lattice images on the angular collecting range of the ADF detector, simulated for the Ge/Si(100) interface. The specimen thickness is 108.3 Å. The mean displacements of the Ge and Si atoms are taken as 0.1 Å.

electrons are accumulated at the angular range of $37 < \beta < 111$ mrad. Also, it is noticed that the relative contrast of Ge/Si changes from 1.69 to 1.86 when the detector angles change from $37 < \beta < 74$ mrad to $74 < \beta < 111$ mrad.

When Eq. (46) was derived, an assumption, namely, the TDS intensity collected by the ADF detector is proportional to the total thermal diffuse scattering if the ADF detector angle is wide, was made. The validity of this assumption can be seen through Fig. 7, because the TDS electrons distributed in the angular range of $\beta < 37$ mrad is a small portion of the total TDS compared to the intensity collected by the detector of $37 < \beta < 111$ mrad. The imaging contrast is then actually dominated by the TDS electrons in the angular range $37 < \beta < 111$ mrad. This is the reason that the calculation based on either the accurate TDS theory [curve *A* in Fig. 6(a)], Eq. (49) [curve *B* in Fig. 6(a)], or Eq. (46) [curve *C* in Fig. 6(a)], gives almost the same contrast distribution.

ADF image contrast depends on the specimen thickness, but not as much as the dependence of the coherent images. It has been shown that the contrast reversal can occur in the ADF image only if the high-order Laue zones (HOLZ) are included by the detector.[29] It is then suggested that the HOLZ effects would be excluded in order to avoid the difficulty of imaging interpretation. Shown in Fig. 8 is a comparison of the relative contrast across the Ge/Si interface for two different specimen thicknesses. The imaging intensity is normalized at a Ge site, as arrowed, for comparison purpose. It is important to note that the relative contrast of the Ge atoms and the Si atoms have been changed for different thicknesses, but no contrast reversal effect is seen for the particular ADF collection angular range.

Changing the focus of the objective lens can change the ADF imaging contrast too, because the probe shape is related to the focus, as seen through Eq. (52b). Shown in Fig. 9 is a comparison of the simulated ADF image contrast across the Ge/Si interface for two different focus cases. Sharp atomic Z-dependent image can be seen for $\Delta f = 800$ Å but reduces quite significantly when

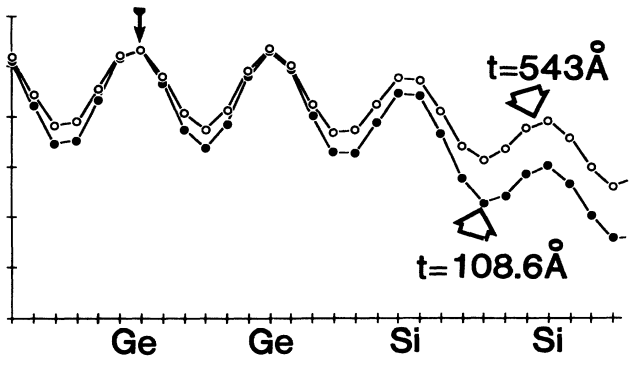

FIG. 8. Dependence of the high-angle ADF STEM lattice images on the specimen thickness, simulated for the Ge/Si(100) interface. The mean displacements of the Ge and Si atoms are taken as 0.1 Å.

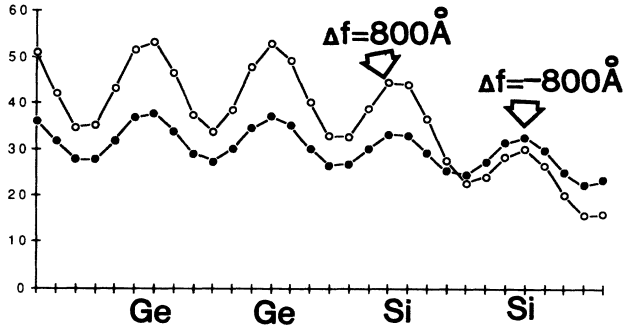

FIG. 9. Dependence of the high-angle ADF STEM lattice images on the focus of the objective lens, simulated for the Ge/Si(100) interface. The specimen thickness is 108.3 Å. The mean displacements of the Ge and Si atoms are taken as 0.1 Å.

$\Delta f = -800$ Å. The image does not show the characteristic of chemical sensitivity when $\Delta f = -800$ Å.

As a summary of ADF image simulation, Eq. (46) and (49) can give almost the exact contrast of the ADF images, therefore they can be used for general ADF image simulations. The ADF image contrast is not affected by the vibration status of the neighboring atoms, that is, the phase of the atomic vibrations [as seen through Eq. (50)], then therefore the image simulation will not be affected by whether assuming the Einstein model, the Debye model, or any other model. The image contrast depends on the collecting angular range of the ADF detector, the specimen thickness, and the focus of the objective lens. No contrast reversal effect is expected if the contribution from HOLZ is excluded. The image contrast cannot be simply predicted using the Z^2 rule, a dynamic calculation for particular ADF detector angular range is required.

VII. DISCUSSIONS AND CONCLUSIONS

Equation (17) is the key equation of the multislice approach, the derivation of which was based on the following approximations: (1) small-angle scattering, i.e., $\alpha^2 \ll 1$; (2) small slice thickness, so that the variation of H'_{nm} in the region $(z - z_0)$ is slow; and (3) small energy loss, $\varepsilon_n \ll E_0$. Conditions (1) and (3) are usually satisfied in high-energy electron diffraction. Condition (2) gives a restriction on the selection of the slice thickness. This situation is similar to the slice-thickness selection in simulating high-resolution electron images. Good accuracy can be obtained by selecting the slice thickness up to a few angstroms. Besides the above conditions, the crystal thickness is also limited. This is because that the error arising from the calculation of the first slice will "propagate" to the later slices, so that the final error is an accumulation of all errors arising from each slice. According to Ishizuka and Uyeda,[13] the slice thickness Δz is restricted by $k\Delta z\alpha^4 \ll 1$, where k is the electron wave vector. This condition is often satisfied. The multislice method, in principle, neglects the back scattering of the electrons, which is usually very weak, especially for high-energy electrons.

The derivation of (17) assumed that the incident electron beam direction is along the z axis. For the nonparallel incidence, (17) also valid apart from replacing σ with $\sigma'=(k/k_z)\sigma$ and propagation function P by $P'=(k_z/k)P$,[36] where k_z is the z component of k. The derivation of Eq. (17) does not assume the three-dimensional periodicity of the crystal structure. This gives the possibility of introducing crystal defects in the calculations. The multislice method can be applied not only for calculating the transmission electron diffraction but also for the reflection electron diffraction in the geometry of glancing angle incidence.

As a conclusion of this paper, a generalized multislice theory is proposed from quantum mechanics to approach the multiple elastic and multiple inelastic scattering of high-energy electrons in a non-perfect crystal. This new theory can provide a substantial basis for characterizing the inelastic scattering of high-energy electrons, such as plasmon excitation, single-electron excitation, and phonon excitation, in a perfect crystal or crystals with defects. Therefore it is a theory of Kikuchi patterns.

The application of this theory to plasmon excitation gives the same answer as obtained from the physical-optics approach. The plasmon scattering becomes important especially in the geometry of reflection electron microscopy (REM), because the spatial variation of the inelastic mean-free path of the electrons can introduce significant effect in the creation of the reflected wave. It has been shown that the inelastic effect can deflect the channelling electrons out of the resonance state and increase the surface reflectance.[37]

The application of the theory for calculating the energy-filtered diffraction patterns of the electrons after exciting the atomic inner shells shows the formation of Kikuchi patterns. These calculations can be compared to the experimental observations if the background effect of the multiple scattered plasmon losses is excluded.

The simulation of high-angle annular-dark-field (ADF) scanning transmission electron microscopy (STEM) images can be approached using the incoherent imaging theory, that is, the image intensity is a thickness integration of the convolution of the electron probe intensity distribution at depth z with the inelastic thermal-diffuse-scattering (TDS) generation function $|G|^2$. This is different from the coherent imaging theory either for TEM or STEM. The TDS can produce atomic resolution lattice images if a small electron probe, less than the unit cell, is used. This image is produced mainly by the localized inelastic scattering from the atomic sites. The ADF image contrast is found to be Z dependent and is capable of providing localized specimen chemical information at sharp atomic interfaces, but a monolayer uncertainty may be introduced.

Dynamical calculations have shown that the contrast of ADF STEM images is dominated by thermal diffuse scattering. The ADF imaging contrast of a row of atoms does not depend on the vibration status of the neighboring atoms but the collecting angular range of the ADF detector, the specimen thickness, and the objective lens focus. Quantitative ADF lattice imaging simulation can be carried out based on Eq. (49) if the thermal mean vibration amplitudes of the atoms at the specified temperature and solid structures are known.

Note added in proof. The "incoherence" of the ADF STEM imaging is suggested by Pennycook and Jesson[38] as the excitation of atomic s states based on pure *elastic* calculations of large-angle Rutherford scattering. It is not surprising to emphasize the contributions of the s states based on their initial assumption that all the large-angle scattering is generated at the nuclear sites.[39] In practice, however, it is believed that the image contrast is dominated by TDS.[29,32] It is obvious that the generation function of TDS [Eq. (50)] is zero at the equilibrium position of each atom,[32] which can produce significant different image contrast from the one expected from the Rutherford scattering model, in which the maximum scattering occurs at the nuclear sites, especially when the size of the electron probe is equal or less than the atom sizes.

As pointed out at the end of Sec. VI A, adding a random number to the inelastic waves generated from different crystal slices cannot effectively characterize the incoherence of the inelastic scattered electrons especially in diffraction calculations. This problem can be solved using a new introduced method for solving Eq. (5) in thin crystal cases.[40]

ACKNOWLEDGMENTS

The author is grateful to Professor J. M. Cowley for his encouragement, support, and many useful discussions. This work was carried out at University of Cambridge and Arizona State University, and partially supported by NSF Grant No. DMR 88-10238 and by the Division of Materials Sciences, U.S. Department of Energy, under Contract No. DE-AC05-840R21400 with Martin Marietta Energy Systems, Inc.

APPENDIX A: DERIVING EQ. (7a) FROM EQ. (6)

Let us first consider the nth inelastic component. By defining U_n as

$$U_n(\mathbf{r})=\sum_m \frac{2m_0}{\hbar^2}H'_{nm}(\mathbf{r})\Psi_m(\mathbf{r}) , \tag{A1}$$

Eq. (5b) can then be written as

$$(\nabla^2+k_n^2)\Psi_n(\mathbf{r})=U_n(\mathbf{r}) . \tag{A2}$$

The solution of (A2) can be found with the Green-function method,

$$G(\mathbf{r}-\mathbf{r}',\mathbf{k}_n)=-\frac{\exp[i(k_n|\mathbf{r}-\mathbf{r}'|)]}{4\pi|\mathbf{r}-\mathbf{r}'|} , \tag{A3}$$

which satisfies

$$(\nabla^2+k_n^2)G(\mathbf{r}-\mathbf{r}',\mathbf{k}_n)=\delta(\mathbf{r}-\mathbf{r}') . \tag{A4}$$

The solution of (A2) can then be written as

$$\Psi_n(\mathbf{r})=\exp[i\mathbf{k}_n\cdot\mathbf{r}]+\int G(\mathbf{r}-\mathbf{r}',\mathbf{k}_n)U_n(\mathbf{r}')d\mathbf{r}' . \tag{A5}$$

Replacing Ψ by $\Phi e^{i\mathbf{k}_n\cdot\mathbf{r}}$ and using (A1), (A5) then becomes

$$\Phi_n(\mathbf{r})=1-\sum_m \frac{2m_0}{4\pi\hbar^2}\int F(\mathbf{r}-\mathbf{r}',\mathbf{k}_n)H'_{nm}(\mathbf{r}')\Phi_m(\mathbf{r}')d\mathbf{r}' , \tag{A6}$$

with

$$F(\mathbf{r}-\mathbf{r}',\mathbf{k}_n)=\frac{\exp\{i[k_n|\mathbf{r}-\mathbf{r}'|-\mathbf{k}_n\cdot(\mathbf{r}-\mathbf{r}')]\}}{|\mathbf{r}-\mathbf{r}'|} . \tag{A7}$$

(A6) is the nth row of Eq. (7a).

APPENDIX B: PROOF OF EQ. (15)

Equation (15) is proved using the method of mathematical induction. First one considers the solution for $L=1$. From (14b),

$$f_1^{(n)}(\mathbf{b},z)=\int\int\int_{z'=z_0}^{z'=z} P_1(\mathbf{b}-\mathbf{b}',z-z') \times\sum_m H'_{1m}(\mathbf{b}',z')\phi_m(\mathbf{b}_0,z_0) \times P_m(\mathbf{b}'-\mathbf{b}_0,z'-z_0) \times d\mathbf{b}_0 d\mathbf{b}' dz' . \tag{B1}$$

By using the method of stationary phase for the integration of propagation function P[13], i.e., for a slow variation function V in the region $(z-z_0)$, one has

$$\int V(\mathbf{b}',z')P_n(\mathbf{b}-\mathbf{b}',z-z')P_n(\mathbf{b}'-\mathbf{b}_0,z'-z_0)d\mathbf{b}' \approx V(\mathbf{b}_0,z')P_n(\mathbf{b}-\mathbf{b}_0,z-z_0) . \tag{B2}$$

Integrating over $\mathbf{b}'$ and assuming the slow variation of the H'_{nm} in the region $(z-z_0)$ as well as $k_1=k_m$, (B1) becomes

$$f_1^{(n)}(\mathbf{b},z)=\int P_1(\mathbf{b}-\mathbf{b}_0,z-z_0) \times\sum_m h'_{nm}(\mathbf{b}_0,\Delta z)\phi_m(\mathbf{b}_0,z_0)d\mathbf{b}_0 . \tag{B3}$$

It is obvious that (B3) is the second row of Eq. (15) for $L=1$. If $f_L^{(n)}$ satisfies (15), then $f_{L+1}^{(n)}$ will be obtained from Eq. (14b),

$$\begin{bmatrix} f_{L+1}^{(0)}(\mathbf{b},z) \\ f_{L+1}^{(1)}(\mathbf{b},z) \\ \vdots \\ f_{L+1}^{(m)}(\mathbf{b},z) \end{bmatrix} = \int d\mathbf{b}'\int_{z'=z_0}^{z'=z} dz' \begin{bmatrix} P_0(\mathbf{b}-\mathbf{b}',z-z') & 0 & \cdots & 0 \\ 0 & P_1(\mathbf{b}-\mathbf{b}',z-z') & \cdots & 0 \\ \vdots & \vdots & \vdots & \vdots \\ 0 & 0 & \cdots & P_m(\mathbf{b}-\mathbf{b}',z-z') \end{bmatrix}$$

$$\times \begin{bmatrix} H'_{00}(\mathbf{b}',z') & H'_{01}(\mathbf{b}',z') & \cdots & H'_{0m}(\mathbf{b}',z') \\ H'_{10}(\mathbf{b}',z') & H'_{11}(\mathbf{b}',z') & \cdots & H'_{1m}(\mathbf{b}',z') \\ \vdots & \vdots & \vdots & \vdots \\ H'_{m0}(\mathbf{b}',z') & H'_{m1}(\mathbf{b}',z') & \cdots & H'_{mm}(\mathbf{b}',z') \end{bmatrix}$$

$$\times \frac{1}{L!}\int d\mathbf{b}_0 \begin{bmatrix} P_0(\mathbf{b}'-\mathbf{b}_0,z'-z_0) & 0 & \cdots & 0 \\ 0 & P_1(\mathbf{b}'-\mathbf{b}_0,z'-z_0) & \cdots & 0 \\ \vdots & \vdots & \vdots & \vdots \\ 0 & 0 & \cdots & P_m(\mathbf{b}'-\mathbf{b}_0,z'-z_0) \end{bmatrix}$$

$$\times \begin{bmatrix} h'_{00}(\mathbf{b}_0,\Delta z') & h'_{01}(\mathbf{b}_0,\Delta z') & \cdots & h'_{0m}(\mathbf{b}_0,\Delta z') \\ h'_{10}(\mathbf{b}_0,\Delta z') & h'_{11}(\mathbf{b}_0,\Delta z') & \cdots & h'_{1m}(\mathbf{b}_0,\Delta z') \\ \vdots & \vdots & \vdots & \vdots \\ h'_{m0}(\mathbf{b}_0,\Delta z') & h'_{m1}(\mathbf{b}_0,\Delta z') & \cdots & h'_{mm}(\mathbf{b}_0,\Delta z') \end{bmatrix}^L \begin{bmatrix} \phi_0(\mathbf{b}_0,z_0) \\ \phi_1(\mathbf{b}_0,z_0) \\ \vdots \\ \phi_m(\mathbf{b}_0,z_0) \end{bmatrix} , \tag{B4}$$

where $\Delta z'=z'-z_0$. Multiplying out the first three matrices in (B4), integrating with respect to $\mathbf{b}'$ using (B2), (B4) becomes (B5).

$$\begin{bmatrix} f_{L+1}^{(0)}(\mathbf{b},z) \\ f_{L+1}^{(1)}(\mathbf{b},z) \\ \vdots \\ f_{L+1}^{(m)}(\mathbf{b},z) \end{bmatrix} = \frac{1}{L!}\int d\mathbf{b}_0 \int_{z'=z_0}^{z'=z} dz' \begin{bmatrix} P_0(\mathbf{b}-\mathbf{b}_0,z-z_0) & 0 & \cdots & 0 \\ 0 & P_1(\mathbf{b}-\mathbf{b}_0,z-z_0) & \cdots & 0 \\ \vdots & \vdots & \vdots & \vdots \\ 0 & 0 & \cdots & P_m(\mathbf{b}-\mathbf{b}_0,z-z_0) \end{bmatrix}$$

$$\times \begin{bmatrix} H'_{00}(\mathbf{b}_0,z') & H'_{01}(\mathbf{b}_0,z') & \cdots & H'_{0m}(\mathbf{b}_0,z') \\ H'_{10}(\mathbf{b}_0,z') & H'_{11}(\mathbf{b}_0,z') & \cdots & H'_{1m}(\mathbf{b}_0,z') \\ \vdots & \vdots & \vdots & \vdots \\ H'_{m0}(\mathbf{b}_0,z') & H'_{m1}(\mathbf{b}_0,z') & \cdots & H'_{mm}(\mathbf{b}_0,z') \end{bmatrix}$$

$$\times \begin{bmatrix} h'_{00}(\mathbf{b}_0,\Delta z') & h'_{01}(\mathbf{b}_0,\Delta z') & \cdots & h'_{0m}(\mathbf{b}_0,\Delta z') \\ h'_{10}(\mathbf{b}_0,\Delta z') & h'_{11}(\mathbf{b}_0,\Delta z') & \cdots & h'_{1m}(\mathbf{b}_0,\Delta z') \\ \vdots & \vdots & \vdots & \vdots \\ h'_{m0}(\mathbf{b}_0,\Delta z') & h'_{m1}(\mathbf{b}_0,\Delta z') & \cdots & h'_{mm}(\mathbf{b}_0,\Delta z') \end{bmatrix}^L \begin{bmatrix} \phi_0(\mathbf{b}_0,z_0) \\ \phi_1(\mathbf{b}_0,z_0) \\ \vdots \\ \phi_m(\mathbf{b}_0,z_0) \end{bmatrix} . \tag{B5}$$

Noting that $h'_{nm} \approx H'_{nm}(z'-z_0)$ for $\Delta z' \to 0$, then integrating by parts in (B5) for z', one obtains

$$\begin{bmatrix} f_{L+1}^{(0)}(\mathbf{b},z) \\ f_{L+1}^{(1)}(\mathbf{b},z) \\ \vdots \\ f_{L+1}^{(m)}(\mathbf{b},z) \end{bmatrix} = \frac{1}{(L+1)!}\int d\mathbf{b}_0 \begin{bmatrix} P_0(\mathbf{b}-\mathbf{b}_0,\Delta z) & 0 & \cdots & 0 \\ 0 & P_1(\mathbf{b}-\mathbf{b}_0,\Delta z) & \cdots & 0 \\ \vdots & \vdots & \vdots & \vdots \\ 0 & 0 & \cdots & P_m(\mathbf{b}-\mathbf{b}_0,\Delta z) \end{bmatrix}$$

$$\times \begin{bmatrix} h'_{00}(\mathbf{b}_0,\Delta z) & h'_{01}(\mathbf{b}_0,\Delta z) & \cdots & h'_{0m}(\mathbf{b}_0,\Delta z) \\ h'_{10}(\mathbf{b}_0,\Delta z) & h'_{11}(\mathbf{b}_0,\Delta z) & \cdots & h'_{1m}(\mathbf{b}_0,\Delta z) \\ \vdots & \vdots & \vdots & \vdots \\ h'_{m0}(\mathbf{b}_0,\Delta z) & h'_{m1}(\mathbf{b}_0,\Delta z) & \cdots & h'_{mm}(\mathbf{b}_0,\Delta z) \end{bmatrix}^{L+1} \begin{bmatrix} \phi_0(\mathbf{b}_0,z_0) \\ \phi_1(\mathbf{b}_0,z_0) \\ \vdots \\ \phi_m(\mathbf{b}_0,z_0) \end{bmatrix} . \tag{B6}$$

It is necessary to point out that the results in (B6) are only valid for Δz is very small. With Eqs. (B3) and (B6) the mathematical induction is completed.

APPENDIX C: CONSERVATION OF TOTAL ELECTRON INTENSITY GOVERNED BY EQ. (17)

From Eq. (17), for the convenience of analytical statement, one defines a transition matrix as

$$T(\mathbf{b}_0,\Delta z) = \begin{bmatrix} h'_{00}(\mathbf{b}_0,\Delta z) & h'_{01}(\mathbf{b}_0,\Delta z) & \cdots & h'_{0m}(\mathbf{b}_0,\Delta z) \\ h'_{10}(\mathbf{b}_0,\Delta z) & h'_{11}(\mathbf{b}_0,\Delta z) & \cdots & h'_{1m}(\mathbf{b}_0,\Delta z) \\ \vdots & \vdots & \vdots & \vdots \\ h'_{m0}(\mathbf{b}_0,\Delta z) & h'_{m1}(\mathbf{b}_0,\Delta z) & \cdots & h'_{mm}(\mathbf{b}_0,\Delta z) \end{bmatrix} . \tag{C1}$$

It can be directly proven from the definition of h'_{nm} that the matrix T has the property

$$T^+ = T , \tag{C2}$$

where $+$ denotes an operation of Hermitian conjugate (i.e., complex conjugate plus matrix transpose). Also the propagation function, defined in Eq. (8b), obeys,

$$\int d\mathbf{b}\, P_n(\mathbf{b}-\mathbf{b}_0,\Delta z) P_n^*(\mathbf{b}-\mathbf{b}_1,\Delta z) = \delta(\mathbf{b}_1-\mathbf{b}_0) . \tag{C3}$$

The total electron intensity after penetrating a crystal slice can then be calculated according to Eq. (17),

$$\sum_{n=0}^{m}\int|\phi_n(\mathbf{b},z)|^2d\mathbf{b}=\int d\mathbf{b}[\phi_0^*(\mathbf{b},z)\phi_1^*(\mathbf{b},z)\cdots\phi_m^*(\mathbf{b},z)]\begin{bmatrix}\phi_0(\mathbf{b},z)\\ \phi_1(\mathbf{b},z)\\ \vdots\\ \phi_m(\mathbf{b},z)\end{bmatrix}$$

$$=\int d\mathbf{b}_1[\phi_0^*(\mathbf{b}_1,z_0)\phi_1^*(\mathbf{b}_1,z_0)\cdots\phi_m^*(\mathbf{b}_1,z_0)]\exp[i\sigma T^+(\mathbf{b}_1,\Delta z)]$$

$$\times\int d\mathbf{b}\begin{bmatrix}P_0^*(\mathbf{b}-\mathbf{b}_1,\Delta z) & 0 & \cdots & 0\\ 0 & P_1^*(\mathbf{b}-\mathbf{b}_1,\Delta z) & \cdots & 0\\ \vdots & \vdots & \vdots & \vdots\\ 0 & 0 & \cdots & P_m^*(\mathbf{b}-\mathbf{b}_1,\Delta z)\end{bmatrix}$$

$$\times\int d\mathbf{b}_0\begin{bmatrix}P_0(\mathbf{b}-\mathbf{b}_0,\Delta z) & 0 & \cdots & 0\\ 0 & P_1(\mathbf{b}-\mathbf{b}_0,\Delta z) & \cdots & 0\\ \vdots & \vdots & \vdots & \vdots\\ 0 & 0 & \cdots & P_m(\mathbf{b}-\mathbf{b}_0,\Delta z)\end{bmatrix}$$

$$\times\exp[i\sigma T^+(\mathbf{b}_0,\Delta z)]\begin{bmatrix}\phi_0(\mathbf{b}_0,z_0)\\ \phi_1(\mathbf{b}_0,z_0)\\ \vdots\\ \phi_m(\mathbf{b}_0,z_0)\end{bmatrix}. \tag{C4}$$

Using Eqs. (C3) and (C1), integrating over $\mathbf{b}$ first, and then over $\mathbf{b}_1$, one gets from (C4)

$$\sum_{n=0}^{m}\int|\phi_n(\mathbf{b},z)|^2d\mathbf{b}=\sum_{n=0}^{m}\int|\phi_n(\mathbf{b},z_0)|^2d\mathbf{b}\ . \tag{C5}$$

That is, the total intensity (elastic plus inelastic) is conserved before and after being scattered by a crystal slice.

---

*Present address: Metals and Ceramics Division, Oak Ridge National Laboratory, Oak Ridge, TN, 37831-6376. (Address for correspondence.)

[1]H. Yoshioka, J. Phys. Soc. Jpn. **12**, 618 (1957).
[2]M. J. Whelan, J. Appl. Phys. **36**, 2099 (1965).
[3]C. J. Humphreys and P. B. Hirsch, Philos. Mag. **18**, 115 (1968).
[4]G. Radi, Acta. Crystallogr. Sect. A **26**, 41 (1970).
[5]H. Yoshioka and Y. Kainuma, J. Phys. Soc. Jpn. **17**, Suppl. BII, 134 (1962).
[6]Z. L. Wang, Acta. Crystallogr. Sect. A (to be published).
[7]A. Howie, Proc. R. Soc. London **271**, 268 (1963).
[8]P. Rez, C. J. Humphreys, and M. J. Whelan, Philos. Mag. **35**, 81 (1977).
[9]P. Rez, Acta. Crystallogr. Sect. A **39**, 697 (1983).
[10]R. Serneels, D. Haentjens, and R. Gevers, Philos. Mag. **42**, 1 (1980).
[11]J. M. Cowley and A. F. Moodie, Acta. Crystallogr. Sect. A **10**, 609 (1957).
[12]P. Goodman and A. F. Moodie, Acta. Crystallogr. Sect. A **30**, 280 (1974).
[13]K. Ishizuka and N. Uyeda, Acta. Crystallogr. Sect. A **33**, 740 (1977).
[14]For example, see P. Self and M. A. O'Keefe, in *High Resolution Transmission Electron Microscopy and Associated Techniques,* edited by P. Buseck, J. M. Cowley, and L. Eyring (Oxford, New York, 1988).
[15]For example, see L. D. Marks, Surf. Sci. **139**, 281 (1984).
[16]Z. L. Wang, P. Lu, and J. M. Cowley, Ultramicroscopy **23**, 205 (1987); Z. L. Wang, *ibid.* **24**, 371 (1988).
[17]Z. L. Wang, J. Liu, P. Lu, and J. M. Cowley, Ultramicroscopy **27**, 101 (1989).
[18]Z. L. Wang, Surf. Sci. **215**, 201 (1989); **215**, 217 (1989).
[19]Z. L. Wang, Acta. Crystallogr. Sect. A **45**, 193 (1989).
[20]For example, see R. Garcia-Molina, A. Gras-Marti, A. Howie, and R. H. Ritchie, J. Phys. C **18**, 5335 (1985).
[21]L. D. Landau and E. M. Lifshitz, *Quantum Mechanics (Non-relativistic Theory)* 3rd ed. (Pergamon, New York, 1977).
[22]R. F. Egerton, *Electron Energy-Loss Spectroscopy in the Electron Microscope* (Plenum, New York, 1986).
[23]H. Bethe, Ann. Phys. **5**, 325 (1933).
[24]For K edge ionization see D. H. Madison and E. Merzbacher, in *Ionization and Transition Probabilities,* Vol. I of *Atomic Inner-Shell Processes,* edited by Bernd Crasemann (Academic, New York, 1975); for L-edge ionization see M. C. Walske, Phys. Rev. **101**, 940 (1956); B. H. Choi, E. Merzbacher, and G. S. Khandelwal, At. Data **5**, 291 (1973).
[25]Z. L. Wang, Acta Crystallogr. Sect. A **45**, 636 (1989).
[26]S. Takagi, J. Phys. Soc. Jpn. **13**, 278 (1958).
[27]M. J. Whelan, J. Appl. Phys. **36**, 2103 (1965).
[28]J. M. Cowley, Acta. Crystallogr. Sect. A **44**, 847 (1988).
[29]Z. L. Wang and J. M. Cowley, Ultramicroscopy, **31**, 437 (1989).
[30]S. J. Penneycook and L. A. Boatner, Nature **336**, 565 (1988).
[31]S. J. Penneycook, EMSA Bulletin **19**, 67 (1989).

[32]Z. L. Wang and J. M. Cowley, Ultramicroscopy (to be published).

[33]L. Reimer and I. Fromm, in Proceeding of the Electron Microscopy Society of America, San Antonio, Texas, 1989, edited by J. Bailey (unpublished), p. 382.

[34]P. A. Doyle, Acta. Crystallogr. Sect. A **27**, 109 (1971).

[35]J. M. Cowley, in *Computer Simulation of Electron Microscopy Diffraction and Images,* edited by W. Krakow and M. O'Keefe (The Minerals, Metals, and Materials Society, Las Vegas, 1989).

[36]K. Ishizuka, Acta. Crystallogr. Sect. A **38**, 773 (1982).

[37]Z. L. Wang, J. Liu, and J. M. Cowley, Acta. Crystallogr. Sect. A **45**, 325 (1989).

[38]J. Pennycook and D. E. Jesson, Phys. Rev. Lett. **64**, 938 (1990).

[39]M. M. J. Treacy, Ultramicroscopy, **26**, 133 (1988).

[40]Z. L. Wang and J. Bentley, in *Proceedings of the 12th International Congress for Electron Microscopy* (Seattle) (San Francisco, CA, in press); Z. L. Wang and J. Bentley, Phys. Rev. B (to be published).

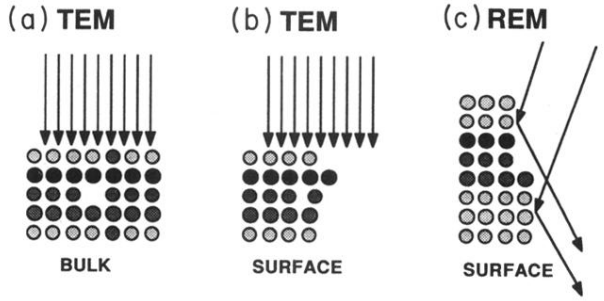

FIG. 2. Application of the multislice theory for simulating (a) the atomic high-resolution transmission electron microscopy (HRTEM) images and convergent beam electron diffraction (CBED) patterns, (b) profile images of surface atomic reconstructions in HRTEM, and (c) reflection electron microscopy (REM) images and reflection high-energy electron diffraction (RHEED) patterns.

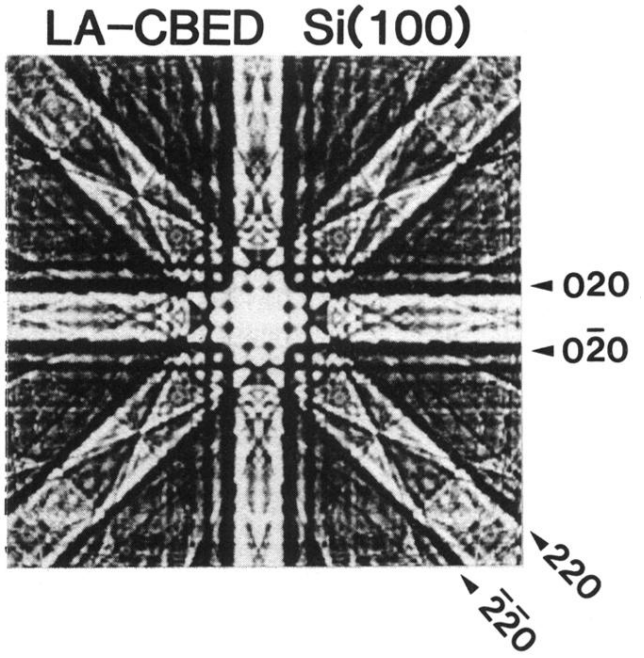

FIG. 3. Simulated large-angle convergent beam electron diffraction LA CBED Kossel pattern of Si(100) for 100-kV electrons, with half-conical angle 6° and specimen thickness 271.5 Å.

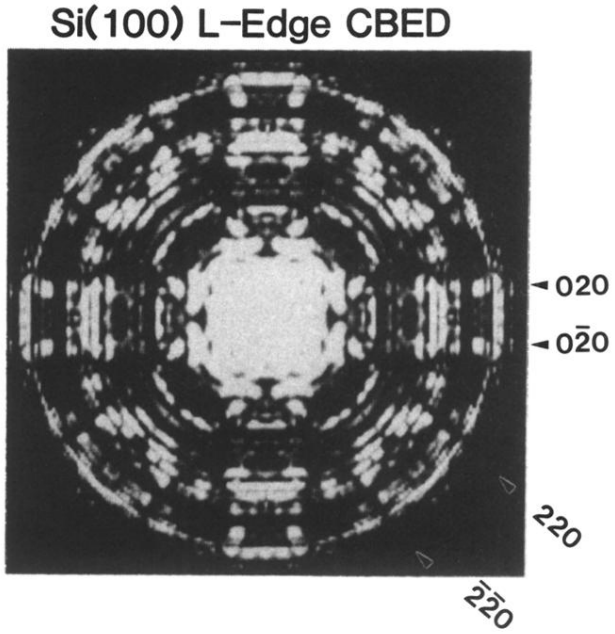

FIG. 4. Simulated energy-filtered Si L-edge core-shell CBED Kikuchi pattern for Si(100), for a specimen thickness 543 Å, beam convergence half-conical angle 12.95 mrad and the energy-loss window $\Delta = 5$ eV above the L edge. This calculation was done by adding arbitrary phases to the inelastic waves generated from different slices.

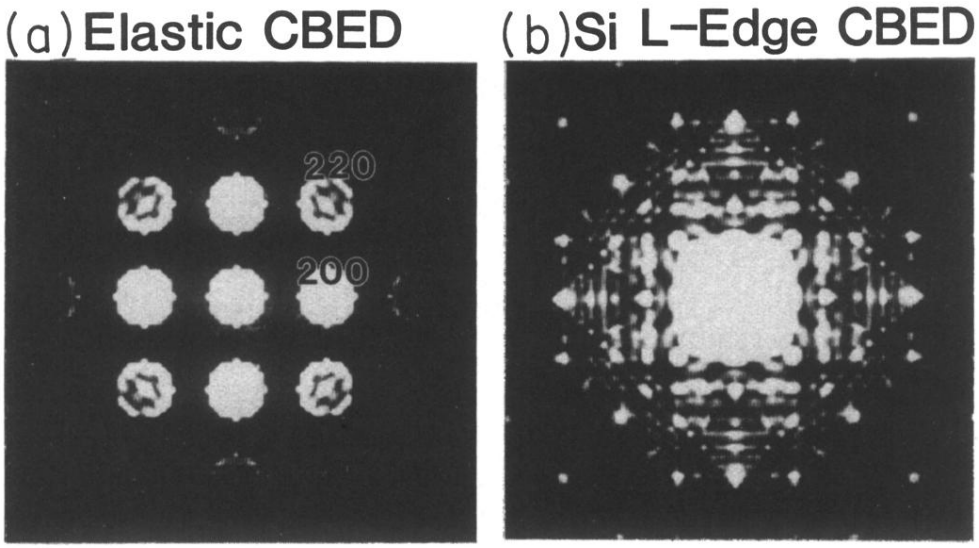

FIG. 5. Simulated Si(100) CBED patterns from (a) elastic scattered electrons and (b) electrons after exciting the Si L edge and then being elastically scattered for 543 Å to form the Kikuchi pattern. The beam convergence half-conical angle is 5.55 mrad and the energy-loss window is $\Delta = 5$ eV above the L edge.